Heterosite Effects in Novel Heteronuclear Clusters $[Os_2Ru(CO)_{11}(PPh_3)]$ and $[Os_2Ru(CO)_{10}$(2-acetylpyridine-*N*-isopropylimine)]

Frank W. Vergeer,[a,e] Martin Lutz,[b] Anthony L. Spek,[b] Maria J. Calhorda,[c,d] Derk J. Stufkens,[†][a] and František Hartl*[a]

Keywords: Cluster compounds / Density functional calculations / Time-resolved spectroscopy / Photochemistry / Spectroelectrochemistry

A new synthetic route towards the mixed-metal cluster $[Os_2Ru(CO)_{12}]$ is described together with the syntheses of its PPh_3 and *i*Pr-AcPy (*i*Pr-AcPy = 2-acetylpyridine-*N*-isopropylimine) derivatives. The molecular structures of the novel clusters $[Os_2Ru(CO)_{11}(PPh_3)]$ and $[Os_2Ru(CO)_{10}$(*i*Pr-AcPy)] were determined on the basis of crystalline solid solutions of the Os_2Ru and corresponding Os_3 species. The structures reveal that coordination of the Lewis bases occurs exclusively at the ruthenium site of $[Os_2Ru(CO)_{12}]$, which is in agreement with density functional theory (DFT) calculations on several structural isomers of these compounds. According to the time-dependent DFT results, the lowest optically accessible excited state of $[Os_2Ru(CO)_{10}$(*i*Pr-AcPy)] has a prevailing σ(Ru–Os2)-π*(*i*Pr-AcPy) character, with a partial σσ*(Ru–Os2) contribution. In weakly coordinating 2-chlorobutane, the excited state has a lifetime τ = 10.4 ± 1.2 ps and produces biradicals considerably faster than observed for $[Os_3(CO)_{10}$(*i*Pr-AcPy) (τ = 25.3 ± 0.7 ps). In coordinating acetonitrile, the excited state of $[Os_2Ru(CO)_{10}$(*i*Pr-AcPy)] decays mono-exponentially with a lifetime τ = 2.1 ± 0.2 ps. In contrast to $[Os_3(CO)_{10}$(*i*Pr-AcPy)] that forms biradicals as the main primary photoproduct even in strongly coordinating solvents, zwitterion formation from the solvated lowest excited state is observed for the heterometallic cluster. This is concluded from time-resolved absorption studies in the microsecond time domain. Due to the lower tendency of the coordinatively unsaturated $^{+}Ru(CO)_2$-(*i*Pr-AcPy$^{-/0}$) moiety to bind a Lewis base, the heteronuclear biradical and zwitterionic photoproducts live significantly shorter than their triosmium counterparts. The influence of the weaker Os2–Ru(*i*Pr-AcPy) bond on the redox reactivity is clearly reflected in very reactive radical anions formed upon electrochemical reduction of $[Os_2Ru(CO)_{10}$(*i*Pr-AcPy)]. The dimer $[^{-}Os(CO)_4$-$Os(CO)_4$-$Ru(CO)_2$(*i*Pr-AcPy)$]_2^{2-}$ is the only IR-detectable intermediate reduction product. The dinuclear complex $[Os_2(CO)_8]^{2-}$ and insoluble $[Ru(CO)_2$(*i*Pr-AcPy)$]_n$ are the ultimate reduction products, proving fragmentation of the Os_2Ru core.

Introduction

In the last four decades, considerable efforts have been made to develop general synthetic routes towards heteronuclear transition metal clusters.[1–4] The interest in this type of clusters where at least one metal–metal bond connects two different core metal atoms, has mainly originated from their possible application in both homogeneous and heterogeneous catalysis.[5] Apart from the general expectation that different transition metal atoms in close proximity of each other could initiate novel reactions by synergistic interactions, the different reactivity of adjacent metal centres in mixed-metal clusters may provide additional bi- or multifunctional activation pathways and increase the selectivity of substrate–cluster interactions.[6] Although catalysis by mixed-metal clusters in a number of cases indeed resulted in higher catalytic activity[7,8] or different product selectivity[9,10] than observed for their homonuclear analogues, the mechanistic insight into the role of the different metal centres in the catalytic cycle is generally limited. This problem mainly has its origin in scarcely available series of isostructural mixed-metal clusters, which precludes a systematic study of their bonding properties and reactivity.

One of the best known series of mixed-metal clusters is the family of group 8 triangular clusters $[M_3(CO)_{12}]$ (M = Fe, Ru, Os), where all possible metal combinations – except $[FeRuOs(CO)_{12}]$ – have been prepared.[3,11] Within this

[†] Deceased.
[a] Van't Hoff Institute for Molecular Sciences, University of Amsterdam,
Nieuwe Achtergracht 166, 1018 WV, Amsterdam, The Netherlands
Fax: +31-20-525-6456
E-mail: f.hartl@uva.nl
[b] Department of Crystal and Structural Chemistry, Utrecht University,
Padualaan 8, 3584 CH Utrecht, The Netherlands
[c] Instituto de Tecnologia Química e Biológica, Av. da República, EAN,
Apart. 127, 2781-901 Oeiras, Portugal
[d] Departamento de Química e Bioquímica, Faculdade de Ciências, Universidade de Lisboa,
1749-016 Lisboa, Portugal
[e] Current address: Physikalisches Institut, Westfälische Wilhelms-Universität Münster,
Wilhelm-Klemm-Strasse 10, 48149 Münster, Germany

series, the clusters $[Os_2Ru(CO)_{12}]$ and $[Ru_2Os(CO)_{12}]$ are of particular interest for our investigations, as the bonding properties, photochemistry and redox behaviour of the homonuclear dodecacarbonyl analogues and, in particular, their α-diimine-substituted derivatives $[M_3(CO)_{10}(\alpha\text{-diimine})]$ (M = Ru, Os), have been studied thoroughly in our groups.[12–21]

A continued systematic study of their heterometallic Ru/Os derivatives is desired in order to reveal the influence of the cluster core variation on the photochemistry and redox reactivity. However, one of the underlying reasons for the lacking studies of $[Os_2Ru(CO)_{12}]$ and $[Ru_2Os(CO)_{12}]$ is the serious difficulty to obtain these clusters in the pure form. Although several synthetic procedures have been reported, they yielded either hardly separable mixtures of $[Ru_3(CO)_{12}]$, $[Ru_2Os(CO)_{12}]$, $[Os_2Ru(CO)_{12}]$ and $[Os_3(CO)_{12}]$ in a nearly statistical 1:2:2:1 ratio[22–24] or gave the desired pure heterometallic clusters merely in very low yields ($\leq$ 5%).[25,26] Development of efficient novel synthetic routes toward these species is therefore compulsory.

Aimed at performing a comparative study of the heteronuclear cluster $[Os_2Ru(CO)_{10}(\alpha\text{-diimine})]$ and its homonuclear analogues $[M_3(CO)_{10}(\alpha\text{-diimine})]$ (M = Ru, Os), a novel route for the synthesis of $[Os_2Ru(CO)_{12}]$ (**1**) has been introduced, producing the cluster in a reasonable yield. Apart from the parent carbonyl cluster, we also report the syntheses and crystal structures of the substituted derivatives $[Os_2Ru(CO)_{11}(PPh_3)]$ (**2**) and $[Os_2Ru(CO)_{10}(i\text{Pr-AcPy})]$ (**3**) (*i*Pr-AcPy = 2-acetylpyridine-*N*-isopropylimine), schematically depicted in Figure 1. Both derivatives were prepared in order to establish the preferential coordination site of different Lewis bases in substitution reactions with $[Os_2Ru(CO)_{12}]$. The influence of the heteronuclear cluster core on the photo- and electrochemical reactivity of $[Os_2Ru(CO)_{10}(i\text{Pr-AcPy})]$ in comparison with the homonuclear derivatives is also described. Density functional theory (DFT) calculations provide direct insight into the bonding properties of $[Os_2Ru(CO)_{11}(PPh_3)]$ and $[Os_2Ru(CO)_{10}(i\text{Pr-AcPy})]$ and support the discussion of the experimental results.

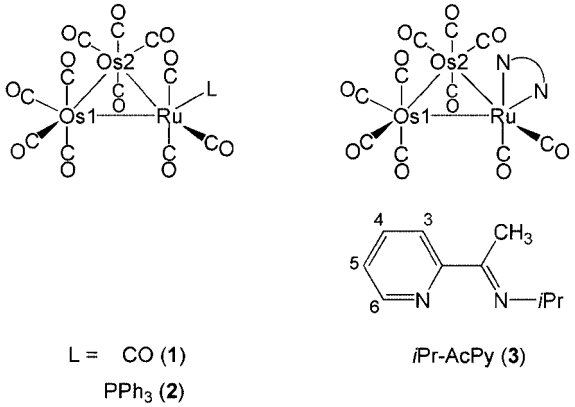

Figure 1. Schematic structures of the investigated clusters $[Os_2Ru(CO)_{11}(L)]$ [L = CO (**1**), PPh_3 (**2**)] and $[Os_2Ru(CO)_{10}(NN)]$ [NN = *i*Pr-AcPy (**3**)].

Results and Discussion

Synthesis of $[Os_2Ru(CO)_{12}]$ (1)

The heteronuclear cluster $[Os_2Ru(CO)_{12}]$ (**1**) was synthesized from its homonuclear analogues $[Os_3(CO)_{12}]$ and $[Ru_3(CO)_{12}]$ in a four-step reaction sequence (Scheme 1). Starting from $[Os_3(CO)_{12}]$, the linear cluster $[Os_3(CO)_{12}(Br)_2]$ was obtained by oxidation with Br_2 in refluxing CH_2Cl_2 [step (*i*)]. After the addition of Br_2, rapid removal of the heating bath is required in order to prevent the reaction of $[Os_3(CO)_{12}(Br)_2]$ with additional Br_2 producing at this stage undesired $[Os_2(CO)_8(Br)_2]$ that is known to transform into $[Os_2(CO)_6(Br)_2]$ at elevated temperatures.[27] Similar oxidative addition of X_2 (X = Cl, Br, I) to $[Ru_3(CO)_{12}]$ was reported[28,29] to yield the mononuclear complex *cis*-$[Ru(CO)_4(X)_2]$ as the initial product, which reflects the increasing stability of the metal–metal bonds towards oxidation on descending the periodic table. Unfortunately, the synthetic strategy depicted in Scheme 1 could therefore not be applied for the synthesis of the isostructural cluster $[Ru_2Os(CO)_{12}]$. The controlled formation of the dinuclear complex $[Os_2(CO)_8(Br)_2]$ was achieved by slight modification of the procedure described by Moss et al. [step (*ii*)].[30] Visible irradiation of $[Os_3(CO)_{12}(Br)_2]$ at $\lambda > 420$ nm was found to prevent excessive formation of the mononuclear complex *cis*-$[Os(CO)_4(Br)_2]$. The latter compound is not only obtained as an unavoidable side-product formed during irradiation of $[Os_3(CO)_{12}(Br)_2]$, but it can also be formed from $[Os_2(CO)_8(Br)_2]$ by UV/Vis irradiation of this complex in the presence of Br_2. In a third step, the powerful nucleophile $Na_2[Ru(CO)_4]$ was prepared from $[Ru_3(CO)_{12}]$ by reduction with sodium in liquid ammonia [step (*iii*)].[31] As $[Ru(CO)_4]^{2-}$ is extremely air- and moisture-sensitive and readily converts to $[Ru(CO)_4H]^-$, the reduction of $[Ru_3(CO)_{12}]$ was performed at reduced pressure (3×10^{-4} Pa) on a high-vacuum line. After the completion of the reaction, the product must be dried extensively, as small traces of ammonia proved to react instantaneously with $[Os_2(CO)_8(Br)_2]$, reducing the yield of $[Os_2Ru(CO)_{12}]$. In order to prevent thermal decomposition of $Na_2[Ru(CO)_4]$ during the drying process, the temperature was carefully kept below 273 K. Finally, $Na_2[Ru(CO)_4]$ was extracted in thoroughly dried THF and added to $[Os_2(CO)_8(Br)_2]$ by vacuum filtration, instantaneously producing $[Os_2Ru(CO)_{12}]$ (**1**) in reasonable yields (step (*iv*)).

Unfortunately, in some cases, cluster **1** was found to contain variable amounts of $[Os_3(CO)_{12}]$ and/or $[Ru_2Os(CO)_{12}]$ impurities. The latter cluster could result from incomplete reduction of $[Ru_3(CO)_{12}]$ by less than six equivalents of sodium. Thus, although the number of impurities and their percentages are significantly reduced in comparison with the established synthetic procedures,[22–24] the purity of cluster **1** and its substitution products remains difficult to control, even when employing this novel synthetic route.

In order to establish the preferred coordination site in cluster **1** for different Lewis bases (L), substituted derivatives with monodentate PPh_3 and chelating α-diimine = *i*Pr-

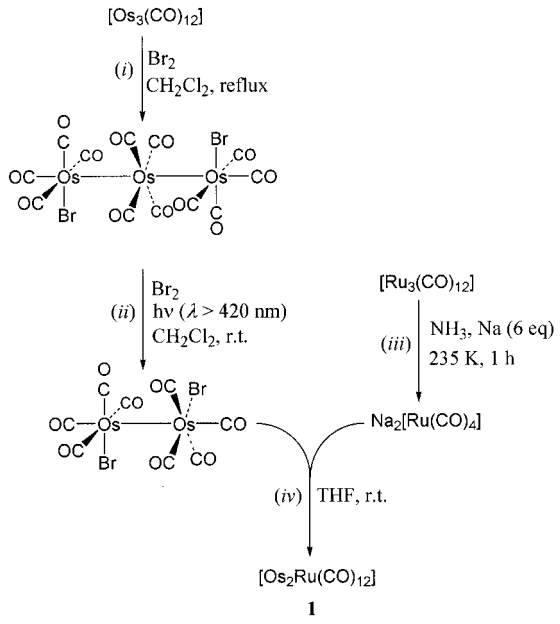

Scheme 1. Synthesis of $[Os_2Ru(CO)_{12}]$ (**1**).

AcPy ligands were prepared by a thermal reaction route involving precursor clusters $[Os_2Ru(CO)_{12-n}(MeCN)_n]$ (n = 1 for L = PPh_3; n = 2 for L = *i*Pr-AcPy). The substituted products $[Os_2Ru(CO)_{11}(PPh_3)]$ (**2**) and $[Os_2Ru(CO)_{10}(i$Pr-AcPy$)]$ (**3**) (see Figure 1) were characterised by IR and NMR spectroscopy and mass spectrometry. Their molecular structures were determined by single-crystal X-ray diffraction and compared with the optimised geometries resulting from DFT calculations.

Molecular Structure of $[Os_2Ru(CO)_{11}(PPh_3)]$ (2)

The crystal structure of cluster **2** is shown in Figure 2. This structure was determined on a mixture of $[Os_2Ru(CO)_{11}(PPh_3)]$ and $[Os_3(CO)_{11}(PPh_3)]$ in a ratio of 0.64:0.36. Selected bond lengths and angles are presented in Table 1. The structure of **2** exhibits disorder amounting to a 36% Os occupancy at the Ru atom site, being significantly distorted from the D_{3h} symmetry observed for $[M_3(CO)_{12}]$ (M = Ru, Os).[32,33] Most importantly, the crystal structure, in combination with (temperature-dependent) ^{31}P NMR spectra, reveals that the PPh_3 ligand in $[Os_2Ru(CO)_{11}(PPh_3)]$ occupies an equatorial position and is exclusively coordinated at Ru. This is in contrast with the results of Pereira et al. who obtained an 1:2 mixture of osmium- and ruthenium-substituted isomers after the reaction of PPh_3 with the tetranuclear mixed-metal cluster $[RuOs_3(\mu\text{-}H)_2(CO)_{13}]$ under similar conditions.[34]

The geometry around the phosphorus atom in cluster **2** is essentially tetrahedral, the phenyl groups being slightly bent away from the Ru atom [C–P–C angles are in the range 100.30(13)–104.64(14)°]. The average metal–metal bond length (2.894 Å) is longer than the unsubstituted homonuclear clusters $[M_3(CO)_{12}]$ [M = Ru: 2.8542 Å;[33] M = Os: 2.8771(27) Å[32]]. This is partly due to the substitution of a

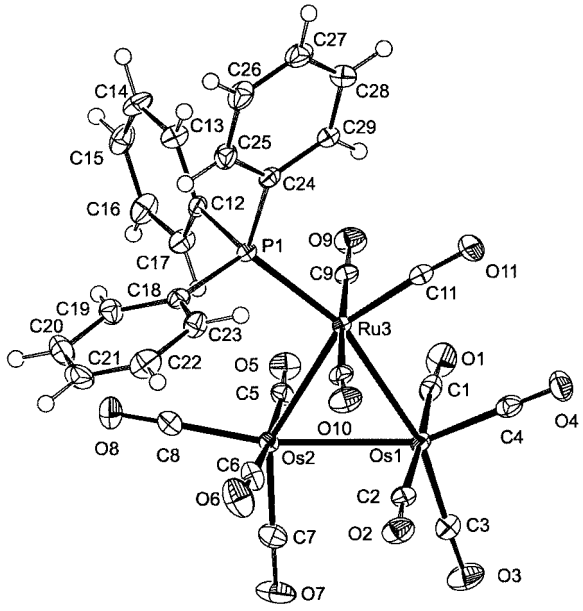

Figure 2. Molecular structure of the cluster $[Os_2Ru(CO)_{11}(PPh_3)]$ (**2**) in the crystal. Displacement ellipsoids are drawn at the 50% probability level. The site of Ru3 is occupied for 64% by Ru and for 36% by Os.

Table 1. Selected bond lengths [Å] and bond angles [°] for cluster **2**, with standard uncertainties in parentheses. For numbering see Figure 2. The site of Ru3 is occupied for 64% by Ru and for 36% by Os.

Ru3–Os1	2.88393(19)	Os1–Ru3–Os2	59.620(4)
Ru3–Os2	2.9147(2)	Os1–Os2–Ru3	59.660(4)
Os1–Os2	2.88275(16)	Ru3–Os1–Os2	60.721(5)
Ru3–P1	2.3683(7)	Ru3–P1–C12	116.70(9)
Ru3–C9	1.939(3)	Ru3–P1–C18	114.07(9)
Ru3–C10	1.940(3)	Ru3–P1–C24	116.04(9)
Ru3–C11	1.887(3)	C12–P1–C18	104.64(14)
P1–C12	1.842(3)	C18–P1–C24	103.18(13)
P1–C18	1.831(3)	C12–P1–C24	100.30(13)
P1–C24	1.826(3)		

π-accepting CO ligand by the much stronger σ-donor PPh_3, increasing the electron density on the metal core and resulting in expansion. Like in the corresponding homonuclear clusters $[M_3(CO)_{11}(PPh_3)]$ (M = Os, Ru),[35,36] the length of the metal–metal bond positioned *cis* to the PPh_3 ligand [Ru–Os2: 2.9147(2) Å] is increased to a larger extent than the other metal–metal bond lengths [Ru–Os1: 2.8839(2) Å; Os1–Os2: 2.8827(2) Å]. This difference has been attributed to steric interactions between the PPh_3 ligand and the *cis*-CO group on the adjacent metal atom.[35,36] The steric and electronic effects are also reflected in the marked shortening of the M–CO_{eq} bond *cis* to the PPh_3 ligand [Ru–C11 = 1.887(3) Å] compared to the average length of these bonds in, for example, $[Ru_3(CO)_{12}]$ [average Ru–CO_{eq}: 1.921(5) Å]. This shortening is ascribed to increased π-back-bonding to the CO ligand, resulting from the presence of the σ-donating phosphorus ligand attached to the same metal and to the sterically induced lengthening of the Ru–Os2 bond *trans* to this CO group.[35]

The Ru–Os bond lenghts [2.9147(2) and 2.8839(2) Å] nicely fit within the values reported for the corresponding metal–metal bond lengths in the homonuclear analogues [$M_3(CO)_{11}(PPh_3)$] [M = Os: 2.918(1) and 2.891(1) Å, M = Ru: 2.907(3) and 2.876(3) Å]. This comparison is possible even though the reported Os–Ru distances do not correspond to "pure" [$Os_2Ru(CO)_{11}(PPh_3)$], but to a blend of Os_2Ru and Os_3 in solid solution (vide supra). The distortion from the D_{3h} symmetry, manifested by the twisting of the $Os(CO)_4$ units, is reflected in the C_{ax}–Os1–Os2–C_{ax} dihedral angles.[35] Just like for the metal–metal bond lengths, the values for C1–Os1–Os2–C5 (3.5°) and C2–Os1–Os2–C6 (12.8°) closely resemble those reported for the homonuclear analogues: 5.4° and 14.4° for Ru and 4.4° and 12.3° for Os, respectively.

The presence of [$Os_3(CO)_{11}(PPh_3)$], which was refined with a substitutional disorder model for the Ru/Os3 atom site, has most likely its origin in the formation of [$Os_3(CO)_{12}$] as a side-product during the preparation of **1** (vide supra). This is also reflected in the mass spectra of some of the [$Os_2Ru(CO)_{12}$] samples where a peak at *m*/*z* 908 is ascribed to the molecular ion of [$Os_3(CO)_{12}$]. The presence of ca. 35% [$Os_3(CO)_{11}(PPh_3)$] is also reflected in the $^{31}P\{H\}$ NMR and FD mass spectra of **2**, indicating that the observed ratio between the Os_3 and Os_2Ru phosphane-substituted clusters in the crystal structure is similar in the gas phase and in solution.

Density Functional Study of [$Os_2Ru(CO)_{11}(PPh_3)$] (2)

The density functional theory (DFT, ADF programme[37–43]) study of cluster **2** was performed with the aim to learn, whether the theory indeed predicts [$Os_2Ru(CO)_{11}(PPh_3)$] to be most stable with the PPh_3 ligand coordinated at the ruthenium centre at an equatorial site. The cluster [$Os_2Ru(CO)_{11}(PH_3)$] (**2a**) served as a model for **2**. Some features of the optimised geometry of **2a** slightly deviate from those of the crystal structure of **2** (Table 2, Figure 3). First of all, the calculated metal–metal bond lengths are slightly longer than the experimental ones (up to 0.05 Å), similar to the situation for [$Os_3(CO)_{12}$].[19,20] The Ru–Os bond *cis* to the PPh_3 ligand is calculated to be significantly longer than the other two metal–metal bonds, in agreement with the crystal structure. This trend points to the role of electronic effects apart from the expected steric influence. For, the differences in the metal–metal bond lengths should be smaller in the model **2a**, as the steric interactions of the PH_3 ligand with the *cis*-CO group on the adjacent metal atom are much less pronounced compared to the bulky PPh_3 ligand. Apart from this feature, the twisting of the $Os(CO)_4$ units in **2a** is much smaller than in the experimental structure. This is reflected in the orientation of the Os–CO_{ax} bonds in **2a**, which are almost perpendicular to the Os_2Ru plane (dihedral angles C1–Os1–Os2–C5 = 0.3° and C2–Os1–Os2–C6 = 0.5°). The larger distortion in the experimental structure has its origin presumably in the phenyl groups of the PPh_3 ligand. In the solid state, these phenyl rings interact with the phenyl rings of the two neighbouring clusters by four edge-to-face interactions to give a one-dimensional chain. Similar interactions, for example, have been reported for the cluster [$Os_3(CO)_{11}\{P(p\text{-}C_6H_4F)_3\}$].[44] Besides the crystal packing effects, not incorporated in the geometry optimisation of **2a**, the twist of the $M(CO)_4$ units also depends on the selected computational basis set.[19]

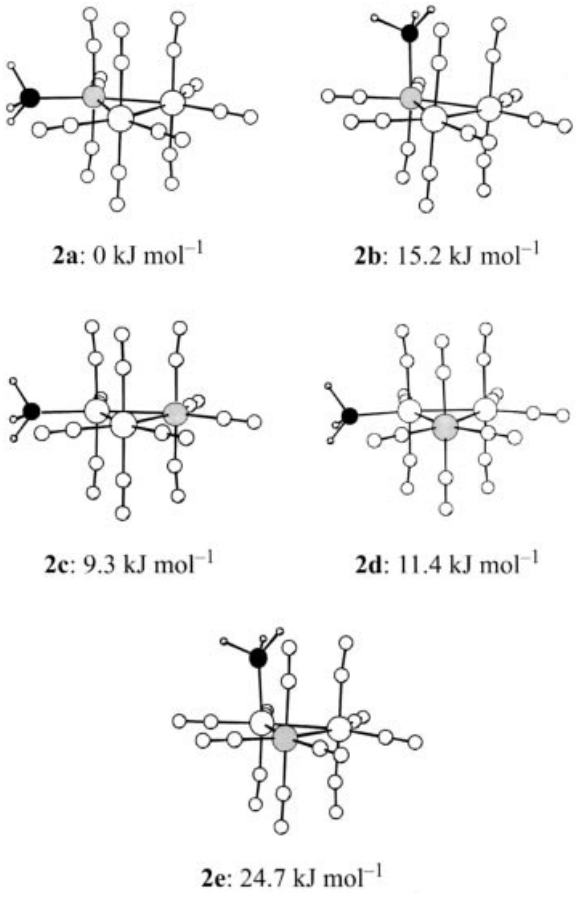

Figure 3. Optimised geometries and relative energies of the model cluster **2a** and its virtual isomers **2b**–**e**.

Table 2. Comparison of selected ADF/BP calculated bond lengths [Å] and angles [°] in cluster **2a** with the experimental crystallographic data.

Bond[a]	Calcd.	Exp.	Angle[a]	Calcd.	Exp.
Ru–Os1	2.913	2.88393(19)	Os1–Ru–Os2	60.0	59.620(4)
Ru–Os2	2.956	2.9147(2)	Os1–Os2–Ru	59.3	59.660(4)
Os1–Os2	2.933	2.88275(16)	Ru–Os1–Os2	60.8	60.721(5)
Ru–P	2.339	2.3683(7)			

[a] See Figure 2.

In addition to the optimised model **2a**, the relative energies of several structural isomers **2b**–**e** have also been calculated (Figure 3). The isomers **2a** and **2b** have in common that the PH_3 ligand is coordinated to ruthenium, but they differ in the coordination of the ligand relative to the Os_2Ru plane (equatorial and axial, respectively). In isomers **2c**–**e**, the PH_3 ligand is coordinated at one of the osmium atoms, **2e** being the only model with the PH_3 ligand coordinated in an axial position. Isomers **2c** and **2d** have the PH_3 ligand coordinated in an equatorial position, but they differ in the orientation of the PH_3 ligand relative to the ruthenium centre. Importantly, isomer **2a** appeared to be more stable by 11.4 kJ·mol^{-1} than isomer **2d**, which proves the preferable coordination of the PH_3 ligand at ruthenium. Isomer **2c**, with the PH_3 ligand perpendicular to the Os1–Os2 bond, is in turn slightly more stable than isomer **2d**, where the position of the PH_3 ligand presents almost a continuation of the Os1–Os2 bond. The isomers **2b** and **2e**, with the PH_3 ligand occupying an axial site at Ru and Os, respectively, are highest in energy.

Although the difference in relative energy between the model structures **2a** and **2c** is relatively small, no experimental evidence has been obtained for $[Os_2Ru(CO)_{11}(PPh_3)]$ clusters with the phosphane ligand coordinated to osmium. However, as the relative energies calculated by DFT refer to isolated gas-phase molecules at zero Kelvin temperature, with PH_3 as the model for the PPh_3 ligand, the obtained values merely reflect a trend in the thermodynamic stability of the different isomers in solution at 293 K.

In order to investigate whether a chelating α-diimine ligand also prefers coordination at the ruthenium site of **1**, we synthesized the cluster $[Os_2Ru(CO)_{10}(i\text{Pr-AcPy})]$ (**3**) and determined its molecular geometry. Apart from its structure, the major interest in cluster **3** stems from our aim to reveal the influence of the heteronuclear cluster core on the photo- and redox reactivity of this compound. For a proper evaluation of this effect, the homonuclear clusters $[Os_3(CO)_{10}(\alpha\text{-diimine})]$ were used as a reference.

Molecular Structure of $[Os_2Ru(CO)_{10}(i\text{Pr-AcPy})]$ (3)

The molecular structure of cluster **3**, determined by single-crystal X-ray diffraction, is shown in Figure 4. Selected bond lengths and angles are collected in Table 3. As in compound **2**, the corresponding Os_3 compound, viz. $[Os_3(CO)_{10}(i\text{Pr-AcPy})]$, was also present in the crystal structure as a solid solution (occupancy 0.89:0.11 for Os_2Ru:Os_3). Importantly, the crystal structure reveals that the *i*Pr-AcPy ligand in $[Os_2Ru(CO)_{10}(i\text{Pr-AcPy})]$ is again bound at the ruthenium atom. Similar to 2,2′-bipyridine (bpy) and *N*,*N*′-diisopropyl-1,4-diaza-1,3-butadiene (*i*Pr-DAB) in the closely related $[Os_3(CO)_{10}(\alpha\text{-diimine})]$ clusters,[45,46] the asymmetric *i*Pr-AcPy ligand is coordinated to a single metal centre in a chelating fashion. The nitrogen atom of the pyridine ring and the imine nitrogen occupy axial and equatorial positions, respectively.

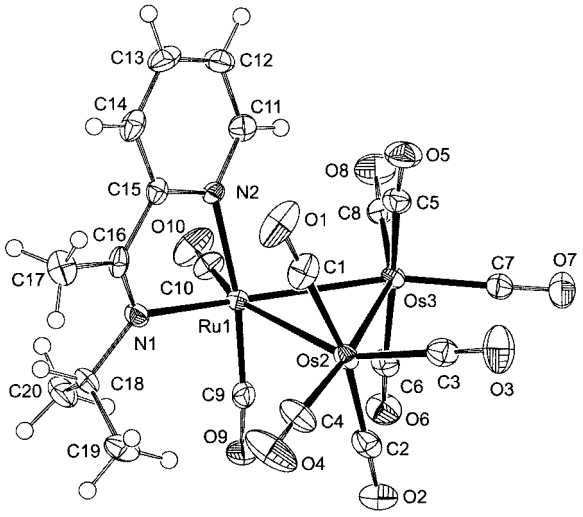

Figure 4. Molecular structure of the cluster $[Os_2Ru(CO)_{10}(i\text{Pr-AcPy})]$ (**3**) in the crystal. Displacement ellipsoids are drawn at the 50% probability level. The site of Ru1 is occupied for 89% by Ru and for 11% by Os.

Table 3. Selected bond lengths [Å] and angles [°] for cluster **3**, with standard uncertainties in parentheses. For numbering see Figure 4. The Ru1 site is occupied for 89% by Ru and for 11% by Os.

Ru1–Os3	2.8694(4)	N1–C16	1.307(5)
Ru1–Os2	2.9159(4)	N2–C15	1.358(5)
Os2–Os3	2.8815(2)		
Ru1–N1	2.141(4)	Os3–Os2–Ru1	59.328(8)
Ru1–N2	2.151(3)	Os2–Os3–Ru1	60.934(8)
Ru1–C9	1.846(5)	Os3–Ru1–Os2	59.738(8)
Ru1–C10	1.855(5)	N1–Ru1–Os3	157.77(10)
N2–C11	1.343(5)	N2–Ru1–Os2	101.98(9)
C11–C12	1.375(6)	N1–Ru1–C9	97.02(16)
C12–C13	1.380(6)	N2–Ru1–C9	171.47(16)
C13–C14	1.385(6)	N1–Ru1–N2	75.25(13)
C14–C15	1.383(6)	N1–C16–C15	115.7(4)
C15–C16	1.470(6)	N2–C15–C16	115.2(4)

Just as for cluster **2**, the observed substitutional disorder due to a small amount of the triosmium analogue most likely has its origin in the formation of $[Os_3(CO)_{12}]$ as a side-product during the preparation of **1**. Apart from the crystal structure, the presence of a small amount of $[Os_3(CO)_{10}(i\text{Pr-AcPy})]$ is also reflected in the FAB$^+$ mass spectrum of **3** where peaks at *m*/*z* 986.9 and 957.9 can be ascribed to $[M^+ - nCO]$ (M = $[Os_3(CO)_{10}(i\text{Pr-AcPy})]$; n = 1, 2). Moreover, the ^{1}H NMR spectrum of **3** in $CDCl_3$ displays small signals at δ = 9.50 (d, 1 H), 8.02 (d, 1 H), 7.86 (dd, 1 H), 7.11 (dd, 1 H) and 4.44 (m, 1 H) ppm, pointing to the presence of ca. 10–15% $[Os_3(CO)_{10}(i\text{Pr-AcPy})]$ (estimated from signal integrals). This proves that the ratio between $[Os_2Ru(CO)_{10}(i\text{Pr-AcPy})]$ and $[Os_3(CO)_{10}(i\text{Pr-AcPy})]$ in solution is very close to that in the solid state.

Density Functional Study of $[Os_2Ru(CO)_{10}(i\text{Pr-AcPy})]$ (3)

DFT calculations (ADF programme[37–43]) were performed in order to obtain more insight into the bonding

properties of **3** and the influence of the Ru atom on the character of the frontier orbitals. The cluster $[Os_2Ru(CO)_{10}(H\text{-}PyCa)]$ (H-PyCa = pyridine-2-carbaldehyde-imine) (**3′**) was taken as a model, with the isopropyl and imine methyl groups of the *i*Pr-AcPy ligand replaced by hydrogen atoms. In order to determine whether the theoretical calculations indeed predict the coordination of *i*Pr-AcPy at the ruthenium centre instead of the osmium sites, the relative energies of the structural isomers **3′** and **3′′** were calculated, with **3′** having the α-diimine coordinated at ruthenium and **3′′** at osmium (Figure 5). In both model systems, H-PyCa is coordinated with the pyridine ring in the axial position. A recent DFT study of the related cluster $[Os_3(CO)_{10}(H\text{-}PyCa)]$[18] has shown that this geometric isomer is more stable than those with the pyridine ring equatorially bound or with both nitrogen atoms coordinated in the equatorial plane.

Geometry optimisation of both isomers with DFT revealed that **3′** is more stable than **3′′** by 22 kJ·mol^{-1}. This is in agreement with the experimental structure, showing that also the *i*Pr-AcPy ligand prefers coordination at the ruthenium site of $[Os_2Ru(CO)_{12}]$. The geometry of model **3′** is in good agreement with the experimental structure of **3** (Table 4, Figure 5).

The relatively large difference between the lengths of the two Ru–N bonds in **3′** (2.05 vs. 2.17 Å) indicates that the α-diimine ligand is coordinated in a more asymmetric fashion than in the experimental structure. The probable reason is the replacement of the isopropyl group by a hydrogen atom, shortening the Ru–N1 bond as a result of different steric and electronic effects.

From the ground-state DFT calculations, the composition of the molecular orbitals of **3′** has been obtained. The

Table 5. Characters and one-electron energies of selected frontier orbitals of $[Os_2Ru(CO)_{10}(H\text{-}PyCa)]$ (**3′**) as calculated by the ADF/BP method (L = LUMO, H = HOMO).

MO		*E* [eV]	Ru	Os1	Os2	H-PyCa	CO
111a	L+2	–2.70	0.5	0.1	0.6	87.7	6.0
110a	L+1	–3.04	23.4	7.3	4.5	9.5	44.6
109a	**L**	**–3.68**	**8.4**	**1.1**	**6.5**	**64.7**	**14.4**
108a	**H**	**–5.28**	**25.5**	**1.0**	**16.7**	**24.9**	**25.4**
107a	H-1	–5.77	24.4	21.9	17.1	3.4	26.7
106a	H-2	–5.84	38.3	16.1	3.2	7.8	30.2
105a	H-3	–6.22	52.8	7.0	10.9	5.8	17.1
104a	H-4	–6.46	35.6	9.6	19.8	1.8	26.5

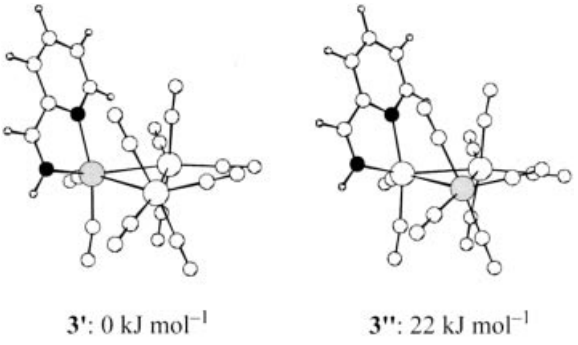

Figure 5. Optimised geometries and relative energies of the model clusters **3′** and **3′′**.

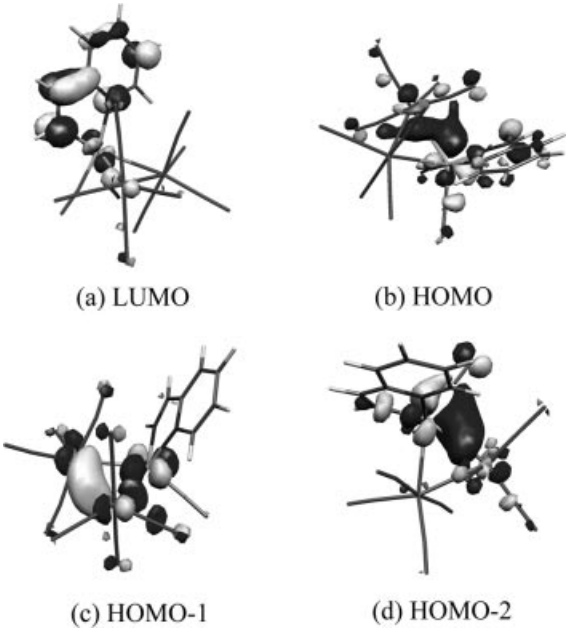

Figure 6. 3D representations of the LUMO (a), HOMO (b), HOMO-1 (c) and HOMO-2 (d) of $[Os_2Ru(CO)_{10}(H\text{-}PyCa)]$ (**3′**).

Table 4. Comparison of selected ADF/BP-calculated bond lengths [Å] and angles [°] in cluster **3′** with the experimental crystallographic data.

Bond[a]	Calcd.	Exp.	Bond/angle[a]	Calcd.	Exp.
Ru–Os3	2.896	2.8694(4)	N1–C16	1.314	1.307(5)
Ru–Os2	2.928	2.9159(4)	N2–C15	1.382	1.358(5)
Os3–Os2	2.913	2.8815(2)			
Ru–N1	2.049	2.141(4)	Os3–Os2–Ru	59.5	59.328(8)
Ru–N2	2.168	2.151(3)	Os2–Os3–Ru	60.5	60.934(8)
N2–C11	1.356	1.343(5)	Os3–Ru–Os2	60.0	59.738(8)
C11–C12	1.385	1.375(6)	N1–Ru–Os3	152.9	157.77(10)
C12–C13	1.405	1.380(6)	N2–Ru–Os3	96.8	97.41(9)
C13–C14	1.383	1.385(6)	N1–Ru–N2	75.2	75.25(13)
C14–C15	1.412	1.383(6)	N1–C16–C15	116.5	115.7(4)
C15–C16	1.426	1.470(6)	N2–C15–C16	113.9	115.2(4)

[a] See Figure 4.

Table 6. TD-DFT calculated lowest-energy singlet excitation energies [eV] and oscillator strengths (O.S.) for $[Os_2Ru(CO)_{10}(H\text{-}PyCa)]$.

Transition	Composition	Energy [eV]	Wavelength [nm]	Exp. λ_{max}[a] [nm]	O.S.
1	63% (H→L); 26% (H-1→L)	2.09	594	581	0.085
2	55% (H-1→L); 23% (H-2→L);	2.16	573		0.021
3	63% (H-2→L); 28% (H→L+1)	2.24	553		0.010
4	49% (H→L+1); 16% (H-3→L); 11% (H→L)	2.46	504	520	0.050
5	76% (H-3→L)	2.63	471	[b]	0.027
6	85% (H→L+2)	2.72	456	[b]	0.020
7	64% (H-4→L); 25% (H-1→L+1)	2.84	436		0.011
8	46% (H-2→L+1); 27% (H-1→L+1)	2.90	428	434	0.038

[a] Absorption maxima of $[Os_2Ru(CO)_{10}(i\text{Pr-}AcPy)]$ observed in hexane at 298 K (Figure 8). [b] Nonresolved.

contribution of the relevant atomic wavefunctions to the frontier orbitals is given in Table 5, with the HOMO (H) and LUMO (L) being in boldface. Three-dimensional plots of the three highest occupied molecular orbitals (HOMO, HOMO-1 and HOMO-2) and of the lowest unoccupied molecular orbital (LUMO), are depicted in Figure 6. Notice that the cluster has a different orientation in Figure 6a–d. The HOMO of **3′** has large contributions from both the Ru and Os2 centres, while Os1 is almost not involved. Accordingly, the HOMO has a σ-bonding character with respect to the Ru–Os2 bond [σ(Ru–Os2)]. All three metal centres participate in the HOMO-1 that is mainly σ-bonding with regard to the Os1 and Os2 centres and will be denoted as σ(Os1–Os2). The Os2 centre is almost not involved in the HOMO-2 that receives large contributions from Ru, Os1 and the carbonyl ligands, being best described as a σ(Ru–Os1) bonding orbital.

The LUMO of **3′** mainly consists of the lowest π*(H-PyCa) orbital, while the LUMO+1 is delocalised over the cluster carbonyl core. Based on the contribution of the atomic wavefunctions to the frontier orbitals, the HOMO–LUMO transition has predominant σ(Ru–Os2)-to-π*(α-diimine) character. A comparison of the frontier orbitals with those of $[Os_3(CO)_{10}(H\text{-}PyCa)]$[18] shows that the HOMOs of both clusters are very similar, with only one specific metal–metal(α-diimine) bond involved in the bonding interactions. Notably, the ruthenium centre in **3′** contributes slightly more (25%) to the HOMO than the corresponding osmium centre in $[Os_3(CO)_{10}(H\text{-}PyCa)]$ (18%). The contributions of the π*(H-PyCa) orbital to the HOMO and the LUMO of both compounds are nearly identical. The excitation energies and the oscillator strengths of the low-lying electronic transitions of **3′** were calculated using TD-DFT and are presented in Table 6.

Electronic Absorption Spectra

The electronic absorption spectra of cluster **3** are characterised by a dominant lowest-energy band showing negative solvatochromism (Table 7) typical for charge transfer (CT) from transition metals to α-diimine ligands.

Table 7. Near-UV and visible absorptions of $[Os_2Ru(CO)_{10}(i\text{Pr-}AcPy)]$ (**3**) in different solvents.

Solvent	λ [nm]
hexane	323 (sh), 434 (sh), 520 (sh), 581
2-chlorobutane	322 (sh), 453 (sh), 562
tetrahydrofuran	323 (sh), 456, 535
acetonitrile	322 (sh), 457, 522

In order to evaluate the solvatochromism of the lowest-energy absorption band, we have plotted the experimentally determined transition energies against the empirical solvent parameter E^*_{MLCT} of Manuta et al. (Figure 7), which is based on the solvatochromism of the lowest MLCT band of $[W(CO)_4(bpy)]$.[47] The plot could be well fitted by linear regression. Its slope reflects the degree of solvatochromism, while the intercept at $E^*_{MLCT} = 0$ corresponds to the experimental transition energy (205.3 kJ·mol^{-1}, 582 nm) extrapolated to nonpolar isooctane interacting similarly weakly with both ground and excited states. The obtained extrapolated value is in good agreement with the calculated maximum of the lowest-energy transition (594 nm, Table 6) and the observed maximum of the lowest-energy absorption band of cluster **3** in hexane (581 nm, Table 7).

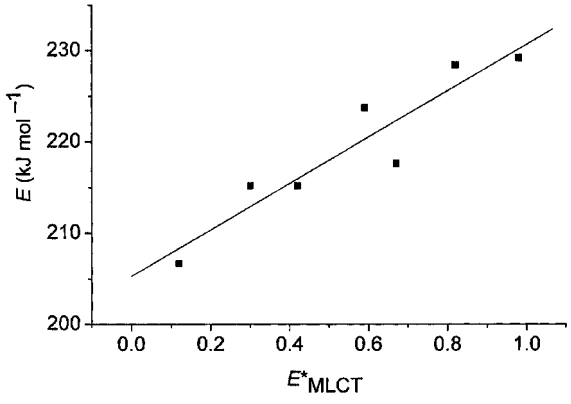

Figure 7. Solvatochromic behaviour of the lowest-energy absorption band of $[Os_2Ru(CO)_{10}(i\text{Pr-}AcPy)]$, based on the empirical solvent scale E^*_{MLCT} according to Manuta et al.[47] The solvents (with E^*_{MLCT} in parentheses) are CCl_4 (0.12), toluene (0.30), $CHCl_3$ (0.42), THF (0.59), CH_2Cl_2 (0.67), acetone (0.82) and acetonitrile (0.98).

The experimental UV/Vis spectrum of cluster **3** in hexane and the corresponding spectrum simulated with SWizard[48] are shown in Figure 8. A comparison between the theoretical and experimental data (Table 6, Table 7 and Figure 8) shows that, besides the lowest-energy absorption band, there is also a good agreement between the calculated maxima of the higher-lying transitions (Table 6), the simulated SWizard spectrum, and the higher-lying band maxima of cluster **3** in hexane (Figure 8). As the absorption features in the visible region are generally broad and poorly resolved, the lowest-energy absorption band of **3** most likely consists of several allowed transitions of a prevailing charge transfer character, which is in line with its solvatochromism. A similar solvent dependence is observed for the higher-lying shoulder at 520 nm that corresponds with the calculated charge-transfer transition 4 (Table 6). The weak shoulder on the low-energy side of the intense near-UV absorption (434 nm in hexane) most likely consists of two differently composed transitions that mainly originate in the cluster core and are directed to the LUMO+1 (transitions 7 and 8, Table 6). Although the calculated excitation energies of the three different groups of electronic transitions (cluster model **3′**) slightly deviate from the experimental values (cluster **3**), the calculated oscillator strengths compare reasonably well with the observed band intensities and clearly predict that the lowest-energy, predominantly HOMO–LUMO transition, is the most intense one in the visible region. Due to their relatively small oscillator strengths and overlap, transitions 5 and 6 (Table 6) do not appear as distinct bands in the UV/Vis spectrum of **3**.

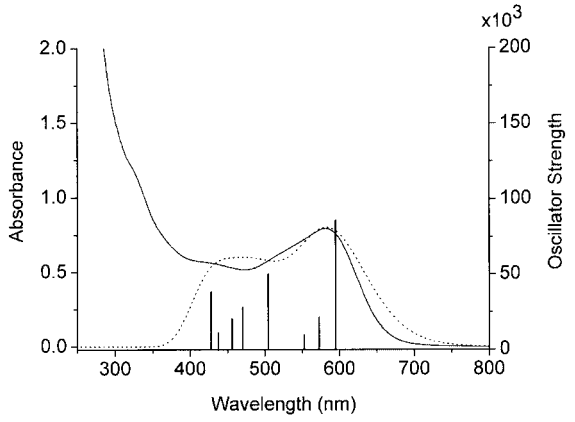

Figure 8. Electronic absorption spectrum of $[Os_2Ru(CO)_{10}(i$Pr-AcPy) in hexane at 293 K (−) together with the simulated SWizard spectrum (···) and the major electronic transitions of cluster **3′**, as calculated with the ADF programme (see Table 6).

Although the experimental results do not reveal whether the lowest-energy charge transfer transition originates from a molecular orbital with a predominant d_π(Ru) character or a delocalised σ(Ru–Os2) character, the TD-DFT results are clearly in favour of the latter assignment. The lowest-energy transition therefore belongs to a σπ* or sigma-bond-to-ligand charge transfer (SBLCT) transition, causing significant weakening of the Ru–Os2 bond in the excited state. Visible excitation of **3** is therefore expected to result efficiently in open-triangle photoproducts such as biradicals and zwitterions.

Time-Resolved Absorption Spectroscopy of Cluster 3 in Noncoordinating Solvents

Picosecond transient absorption (TA) spectra of cluster **3** were recorded in 2-chlorobutane (2-ClBu). Spectral changes following the 505 nm excitation were monitored in the region 510–710 nm. The spectra measured at 1–40 ps after the 130 fs laser pulse are depicted in Figure 9. Kinetic traces were obtained by plotting against time the ΔA values averaged over a small nanometer range. Due to the poor quality of the spectra, reliable lifetimes could only be obtained from the decay in the region 565–580 nm.

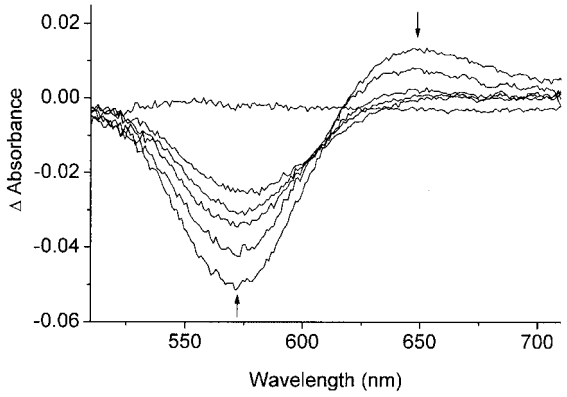

Figure 9. Transient difference absorption spectra of cluster **3** in 2-ClBu, recorded at time delays of –4 (baseline), 1, 3.5, 8.5, 16 and 31 ps, after 505 nm excitation (130 fs FWHM).

The TA spectrum at t_d = 1 ps (Figure 9) shows a bleach at about 570 nm, very close to the maximum of the ground-state absorption of the cluster in this solvent (562 nm), and an absorption with a maximum at 645 nm. The bleach partly disappears with a lifetime of 10.4 ± 1.2 ps. The remaining TA spectrum obtained at t_d = 31 ps, shows a bleach at 580 nm, which is approximately 47% of the initial signal and does not change significantly in the ps time domain. Thus, at least part of the transient species does not regenerate the parent cluster but instead converts into a second species. This is also evidenced by the long-wavelength absorption that transforms on the same time scale as the decay of the bleach into a much broader absorption without a distinct maximum. The ps TA spectra strongly resemble those of $[Os_3(CO)_{10}(i$Pr-AcPy)] in 2-ClBu.[16] This observation also implies that the 11% impurity of the latter cluster in the studied sample of **3** (vide supra) can hardly be distinguished by the TA method in this solvent.

In agreement with the results of the TD-DFT study, the initially observed broad transient absorption above 600 nm is assigned to an excited state having a predominant σπ* character. In this state, one electron has been transferred from the σ(Ru–Os2) bonding orbital (vide supra) to the lowest π* orbital of the *i*Pr-AcPy ligand. Such absorptions are characteristic for complexes in metal-to-α-diimine excited states[49–52] and for α-diimine radical anions contain-

ing at least one aromatic group.[49,53,54] The remaining transient absorption in 2-ClBu is very similar to that observed in the ns TA spectra of **3** (vide infra) and is assigned to the biradical [˙Os(CO)$_4$–Os(CO)$_4$–$^+$Ru(CO)$_2$(α-diimine$^{\cdot-}$)], in accordance with the results for [Os$_3$(CO)$_{10}$(*i*Pr-AcPy)].[16] This assignment has also been verified by recording the ps TA spectra at 250, 500 and 750 ps delays after the laser pulse. These spectra do not differ from that obtained at t_d = 31 ps, thereby proving that the biradicals formed directly from the σπ* excited state do not disappear on the picosecond time scale. Although the TA spectra of **3** in 2-ClBu are very similar to those of the corresponding triosmium cluster, the excited-state lifetime of the former complex is significantly shorter (Os$_3$: τ = 25.3 ps vs. Os$_2$Ru: τ = 10.4 ps). This may be due to the fact that the Os2–Ru(α-diimine) bond is weaker and, thus, the energetic barrier for the biradical formation is lower. Assuming similar molar absorbance for the homo- and heteronuclear biradicals, the higher intensity of the remaining transient signal after the decay of the excited state (Os$_3$: 30% vs. Os$_2$Ru: 47%) also points to a more facile formation of the open-structure photoproducts in the case of cluster **3**.

The fate of the biradicals was studied in several weakly coordinating solvents (2-ClBu, THF, acetone) by nanosecond transient absorption (ns TA) spectroscopy. Spectra of **3** in acetone were obtained by excitation at 532 nm and the spectral changes were monitored in the 350–800 nm region. The difference absorption spectra, measured 0–900 ns after the laser pulse, are depicted in Figure 10. Kinetic traces were recorded after excitation at 532 nm and probed at 560 nm (bleach). The resulting lifetimes are collected in Table 8, together with the values for the corresponding homonuclear cluster [Os$_3$(CO)$_{10}$(*i*Pr-AcPy)].

The ns TA spectra of **3** in acetone reveal a strong bleaching between 440 and 600 nm due to the disappearance of **3**, and transient absorption below 440 nm and in the long-wavelength region. As stated above, the transient absorption is characteristic for α-diimine radical anions[49–52] and for α-diimine complexes in their metal-to-α-diimine excited state, provided the α-diimine ligand bears at least one heteroaromatic group.[49,53,54] As the ns TA spectra closely resemble those of [Os$_3$(CO)$_{10}$(*i*Pr-AcPy)] in acetone,[15] the transient absorption is again assigned to the open-structure biradical [˙Os(CO)$_4$–Os(CO)$_4$–$^+$Ru(Sv)(CO)$_2$(*i*Pr-AcPy$^{\cdot-}$)] (Sv = acetone). In addition, the ns TA spectrum at t_d = 5 ns in acetone is very similar to the TA spectrum of **3** at t_d = 31 ps in 2-ClBu. This confirms that the biradicals formed directly from the excited state, are present in both the ps and ns time domain. The decay of the nanosecond transient species in acetone almost completely regenerated the parent cluster with a lifetime of 228 ns. On changing the solvent to THF and 2-ClBu, the lifetime decreased to 95 and 27 ns, respectively. This result demonstrates that the lifetime of the biradical follows the coordinating ability of the solvent, increasing in the order 2-chlorobutane < THF < acetone. A further increase in the lifetime was found when **3** was irradiated in 2-ClBu in the presence of 1.0 M MeCN. The kinetic trace of this solution shows a decrease of the bleach on the μs time scale (τ = 6.8 μs), but not its complete disappearance. This means that the MeCN-stabilised biradicals did not convert back to the parent cluster but transformed into the corresponding MeCN-stabilised zwitterions, just as observed for [Os$_3$(CO)$_{10}$(*i*Pr-AcPy)].[16] In the case of the triosmium cluster, this process typically occurs for strong Lewis bases (MeCN, pyridine) and firmly coordinating olefins (styrene, octene).[15]

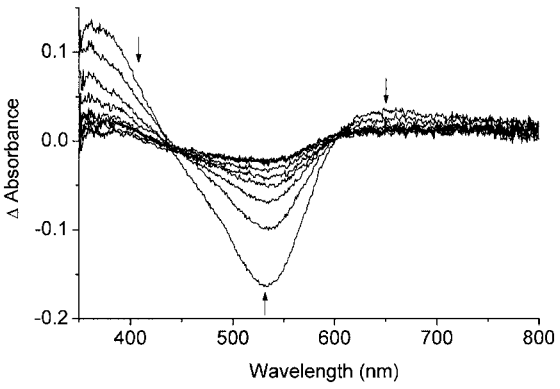

Figure 10. Nanosecond transient difference absorption spectra of cluster **3** in acetone, recorded in the time interval t = 0–900 ns after the 532 nm laser pulse; the time delay between the spectra is 100 ns.

Time-Resolved Spectroscopy in Strongly Coordinating Solvents

In addition to the experiments in 2-ClBu, ps TA spectra of cluster **3** were also recorded in strongly coordinating MeCN. The spectra measured at 1–5 ps after the 130 fs/505 nm laser pulse are depicted in Figure 11. Kinetic traces were extracted by plotting against time the ΔA values averaged in the range 605–615 nm.

Table 8. Lifetimes [ns] of the solvent-stabilised biradical photoproducts of cluster **3** and the reference compound [Os$_3$(CO)$_{10}$(*i*Pr-AcPy)], obtained from their kinetic profiles probed at 560 nm. Standard deviations are given in parentheses.

Solvent	[Os$_2$Ru(CO)$_{10}$(*i*Pr-AcPy)]	[Os$_3$(CO)$_{10}$(*i*Pr-AcPy)]
2-chlorobutane	27(4)	22(3)
THF	95(4)	104(7)
Acetone	228(8)	677(2)
2-chlorobutane/MeCN (1.0 M)	6.8 (0.1)[a]	13.5 (0.2)[a]

[a] Lifetime in μs.

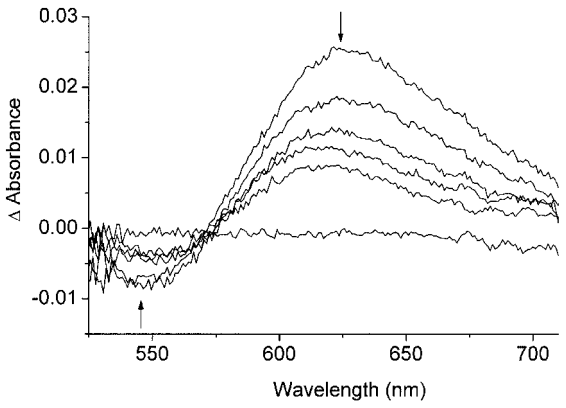

Figure 11. Transient difference absorption spectra of cluster **3** in MeCN, recorded at time delays of –1 (baseline), 1, 1.5, 2.5, 3.5 and 4.5 ps, respectively, after 505 nm excitation (130 fs FWHM).

The first TA spectra (Figure 11) are similar to those in 2-ClBu although the maxima of the bleach (550 nm) and the transient absorption (630 nm) are somewhat shifted. Although the TA spectra of **3** in MeCN resemble those obtained for $[Os_3(CO)_{10}(i\text{Pr-AcPy})]$ in this solvent,[16] the excited states of both clusters behave differently. For $[Os_3(CO)_{10}(i\text{Pr-AcPy})]$ the decay of the excited state in coordinating MeCN is bi-exponential. The slower process (τ = 21.4 ps) has been ascribed to biradical formation, having a lifetime similar to that observed in 2-ClBu.[16] The faster process (τ = 2.9 ps) has been assigned to the heterolytic cleavage of an Os–Os(α-diimine) bond from an MeCN-coordinated excited state with concomitant zwitterion formation; zwitterions were indeed observed in the ps TRIR spectra of $[Os_3(CO)_{10}(i\text{Pr-AcPy})]$.[55] The excited state of cluster **3** decays mono-exponentially in MeCN and its lifetime (τ = 2.1 ps) closely corresponds to the shorter 2.9 ps component of the bi-exponential decay of the excited state of $[Os_3(CO)_{10}(i\text{Pr-AcPy})]$. This points to the same process for both clusters and suggests that irradiation of **3** in neat MeCN gives rise to very fast formation of zwitterions as the only photoproduct. As will be shown hereinafter, TA studies in the nano- and microsecond time domain and rapid scan FTIR spectroscopic measurements confirm this presumption.

As described above, the kinetic trace of **3** in 2-ClBu in the presence of 1.0 M MeCN showed a decrease of the bleach on the μs time scale (τ = 6.8 μs) that, in accordance with the results for $[Os_3(CO)_{10}(i\text{Pr-AcPy})]$,[16] was assigned to the conversion of MeCN-stabilised biradicals into the corresponding MeCN-zwitterions. The MeCN-stabilised biradicals result in this case from the substitution of weakly coordinating 2-ClBu by MeCN within the lifetime of the solvent-stabilised biradicals $[^{\cdot}Os(CO)_4–Os(CO)_4–Ru^+(Sv)(CO)_2(i\text{Pr-AcPy}^{\cdot-})]$ (Sv = 2-ClBu). In neat MeCN, however, the kinetic trace of **3** does not show any change in signal intensity on the nano- and microsecond time scale (Figure 12), indicating that the pathway for zwitterion formation via the biradicals, similar to that observed for the triosmium analogue, does not exist. Thus, contrary to $[Os_3(CO)_{10}(i\text{Pr-AcPy})]$, cluster **3** affords a single photoproduct that does not convert into another species in the time domains studied. Based on our previous ns-μs TA studies of biradical and zwitterion photoproducts of $[Os_3(CO)_{10}(i\text{Pr-AcPy})]$ in MeCN,[12,15,16] the presence of 11% impurity of the latter cluster in the investigated sample of **3** should result in ΔA ca. 0.002 in Figure 12, which is difficult to resolve in the spectral noise.

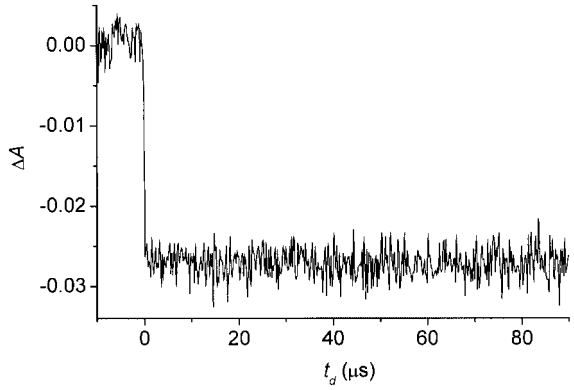

Figure 12. Transient kinetics at 560 nm measured for cluster **3** in MeCN, following irradiation at 532 nm with a Nd:YAG laser (7 ns FWHM, average of 10 shots at 10 s intervals, 2 mJ·pulse^{-1}).

In order to confirm that the single photoproduct is the zwitterion $[^{-}Os(CO)_4–Os(CO)_4–Ru^+(MeCN)(CO)_2(i\text{Pr-AcPy})]$, the photoreaction of **3** in MeCN was followed with rapid-scan IR spectroscopy in the (sub)second time domain. In addition, also pyridine was used as the solvent. Cluster **3** was irradiated for 2 s with an argon-ion laser (514.5 nm, 150 mW) and the IR spectral changes in the CO-stretching region were monitored in both solvents on the time scale of seconds to minutes. The difference IR spectra of **3** in pyridine, measured 0–93 s after the laser pulse, are depicted in Figure 13. Unfortunately, irradiation of **3** in MeCN at 293 K only resulted in the formation of very weak transient bands at 1997 (vw), 1970 (s) and 1874 (s, br) cm^{-1}, that decayed with a lifetime similar to that of the zwitterions formed upon irradiation of $[Os_3(CO)_{10}(i\text{Pr-AcPy})]$ (τ = 38 ± 1 s).[12] Based on the intensity of the transient signals and the observed lifetime, this transient species is assigned as the homonuclear zwitterion $[^{-}Os(CO)_4–Os(CO)_4–{}^{+}Os(MeCN)(CO)_2(i\text{Pr-AcPy})]$, originating from the 11% $[Os_3(CO)_{10}(i\text{Pr-AcPy})]$ impurity in the sample (vide supra). Repeating the experiment at 273 K resulted in similar, more intense product bands, whose decay was clearly bi-exponential. Both the transient absorptions and the parent bleaches rapidly decay within 5 s to approximately 15% of their initial intensity. In a second, slower process, the remaining transient fully regenerates the parent cluster with a lifetime of 54.6 ± 1.2 s, being very close to the lifetime of the zwitterions formed upon irradiation of pure $[Os_3(CO)_{10}(i\text{Pr-AcPy})]$ under these conditions. As the amplitudes of both processes nicely correspond with the observed ratio between $[Os_2Ru(CO)_{10}(i\text{Pr-AcPy})]$ and $[Os_3(CO)_{10}(i\text{Pr-AcPy})]$ in the ^{1}H NMR spectrum and crystal structure of **3**, the faster process is assigned to the decay of

the heteronuclear zwitterions [$^{-}$Os(CO)$_4$–Os(CO)$_4$–$^{+}$Ru(MeCN)(CO)$_2$(*i*Pr-AcPy)]. In agreement with the lifetime, the slower process is then attributed to the decay of the homonuclear zwitterions originating from the [Os$_3$(CO)$_{10}$(*i*Pr-AcPy)] impurity.

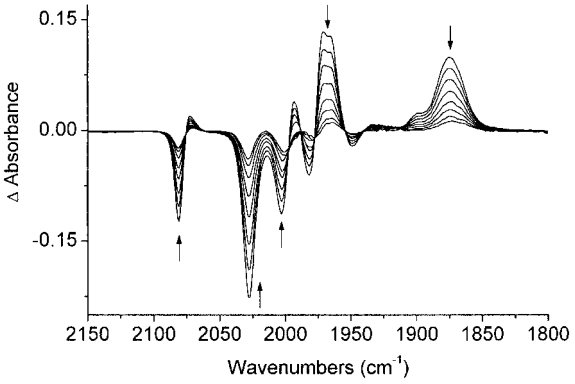

Figure 13. Difference rapid-scan IR spectra of cluster **3** in pyridine measured at time delays of 1.8, 6.6, 11.4, 18.6, 28.2, 40.2, 59.4 and 93.0 s after the 514.5 nm laser pulse.

Irradiation of **3** in strongly coordinating pyridine at room temperature resulted in similar spectral changes as observed in MeCN at 273 K (Figure 13). After excitation, the first spectra display instantaneous bleaching of the parent ν(CO) bands, together with transient absorption bands at 2073 (vw), 1994 (w), 1971 (s), 1965 (sh), 1898 (sh) and 1875 (s, br) cm^{-1}. Both the transient bands and parent bleaches decay again bi-exponentially. The lifetime of the heteronuclear zwitterion increased from a few seconds in MeCN to 23.0 ± 0.3 s in pyridine, which is consistent with the stronger coordination of the latter solvent. At the same time, the difference in the lifetimes of the heteronuclear and triosmium zwitterions has also increased significantly, the latter one living in pyridine for more than 30 minutes. The rapid-scan FTIR experiments thus clearly demonstrate that the irradiation of [Os$_2$Ru(CO)$_{10}$(*i*Pr-AcPy)] in strongly coordinating solvents like MeCN and pyridine results in the formation of solvent-stabilised zwitterions, with lifetimes much shorter than those of the corresponding triosmium zwitterions. The results of the combined time-resolved studies of cluster **3** are summarised in Scheme 2.

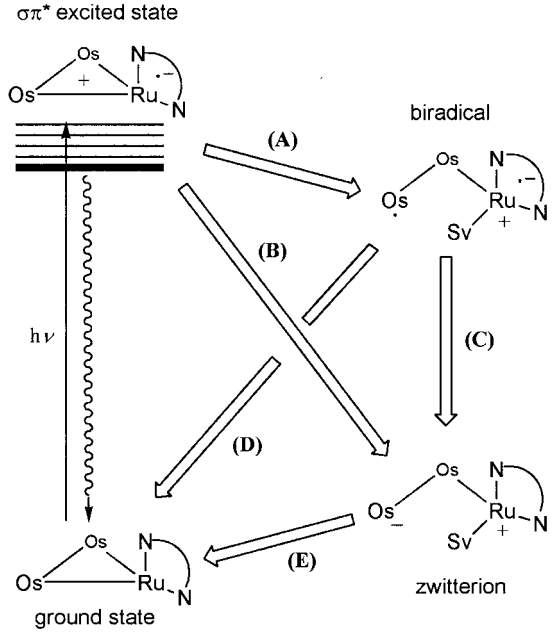

Scheme 2. Schematic representation of the photoreaction pathways established for the cluster [Os$_2$Ru(CO)$_{10}$(*i*Pr-AcPy)] (**3**). The separate reaction steps (**A**)–(**E**) depend on the solvent (Sv) used: (*i*) (**A**) + (**D**) in 2-ClBu, THF, acetone (293 K); (*ii*) (**B**) + (**E**) in MeCN; (*iii*) (**A**) + (**C**) + (**E**) in 2-ClBu + 1.0 M MeCN.

Stability of the Photoproducts

The observed photochemical reactivity of **3** differs significantly from that of the homonuclear clusters [Ru$_3$(CO)$_8$(μ-CO)$_2$(α-diimine)].[17] Although visible excitation of the latter clusters also resulted in the formation of open-structure photoproducts like biradicals and zwitterions, the efficiency of these processes is significantly lower due to the persistent presence of bridging carbonyl ligands in the excited state. Secondly, the triruthenium photoproducts could only be stabilised at low temperatures or in the presence of strongly coordinating Lewis bases or radical scavengers. Regarding the formation of open-structure photoproducts, the photoreactivity of **3** resembles more closely that of its triosmium analogue [Os$_3$(CO)$_{10}$(*i*Pr-AcPy)], for which fairly stable solvent-stabilised biradicals and zwitterions were observed upon excitation into its lowest-energy electronic transition.[12,15,16,55] The latter cluster therefore serves as a reference compound in order to evaluate the influence of the heteronuclear cluster core in **3** on the photoreactivity.

Interestingly, the solvent-stabilised biradicals of parent cluster **3** are significantly shorter-lived than their triosmium counterparts (Table 8). This difference in the biradical lifetime is most striking in acetone, where the lifetime of the heteronuclear biradical (τ = 228 ns) is merely 30% of the value found for [Os$_3$(CO)$_{10}$(*i*Pr-AcPy)] (τ = 677 ns). A much smaller difference is observed in THF (Os$_2$Ru: τ = 95 ns vs. Os$_3$: τ = 104 ns) while in weakly coordinating 2-ClBu the biradical lifetimes of both clusters are almost identical. These results clearly document that the difference in the biradical lifetime increases with the coordinating ability of the solvent. A similar trend applies for the lifetimes of the solvent-stabilised zwitterions. Whereas the lifetime of the heteronuclear zwitterion increases only slightly from a few seconds in MeCN to 23 s in pyridine, the lifetime of the triosmium zwitterion in pyridine amounts to more than 30 minutes compared to 38 s in MeCN. The shorter lifetimes of the heteronuclear photoproducts in better coordinating solvents indicate that the stabilisation of these products by solvent coordination is significantly reduced compared to the corresponding triosmium species. This is attributed to the higher tendency of the coordinatively unsaturated $^{+}$Os(CO)$_2$(*i*Pr-AcPy$^{\cdot-/0}$) moieties in the photoproducts to bind a Lewis base. A similar difference in Lewis base coordination on descending a transition metal group in the peri-

odic table is observed, for example, for the coordinatively unsaturated radicals $[M(CO)_3(\alpha\text{-diimine})]\cdot$ (M = Mn, Re; α-diimine is, e.g., bpy, *i*Pr-PyCa, *i*Pr-DAB). Thus, while the unsaturated radicals $[Re(CO)_3(\alpha\text{-diimine})]\cdot$ form at room temperature fairly stable 18e paramagnetic species $[Re(CO)_3(\alpha\text{-diimine})(Sv)]\cdot$ (Sv = MeCN, PrCN),[56–58] analogous radicals were not observed for $[Mn(CO)_3(\alpha\text{-diimine})]\cdot$.[59]

Redox Behaviour of $[Os_2Ru(CO)_{10}(i\text{Pr-AcPy})]$ (3)

A combined cyclic voltammetric and IR spectroelectrochemical study of cluster **3** was performed in order to investigate the influence of the heteronuclear cluster core on the reduction pathway and stability of the reduction products. The redox potentials are presented in Table 9.

Table 9. Redox potentials of cluster **3** and its reduction products.

Cluster[a][b]	$E_{p,c}$ [V][c]	$E_{p,a}$ [V][c]
3	–1.87 (irr)	+0.27 (irr)
3[d]	–1.93 (irr)	+0.37 (irr)
$\mathbf{3b}^{2-}$ [d]		–1.50 (irr)
$[\mathbf{3b\text{-}3b}]^{2-}$		–1.17 (irr)
$[\mathbf{3b\text{-}3b}]^{2-}$ [d]		–0.85 (irr)

[a] Conditions and definitions: 10^{-3} mol·dm^{-3} solutions in THF (containing 10^{-1} M Bu_4NPF_6) at 293 K, unless stated otherwise; Pt disk microelectrode (0.42 mm^2); v = 100 mV s^{-1}; redox potentials vs. $E_{1/2}$ (Fc/Fc$^+$); $E_{p,c}$, cathodic peak potential for reduction of parent cluster; $E_{p,a}$, anodic peak potential for oxidation of parent cluster or its reduction products. [b] Assignments given in the main text. [c] Chemical irreversibility denoted by (irr). [d] T = 200 K.

The cyclic voltammogram of **3** in THF at room temperature (v = 100 mV·s^{-1}) showed a chemically irreversible two-electron reduction at $E_{p,c}$ = –1.87 V (cathodic peak R_1, see Figure 14a), most likely producing the open-core dianion $[^{-}Os(CO)_4\text{–}Os(CO)_4\text{–}Ru^{-}(CO)_2(i\text{Pr-AcPy})]^{2-}$ ($\mathbf{3b}^{2-}$). Similar dianions are formed upon reduction of the homonuclear clusters $[M_3(CO)_{10}(\alpha\text{-diimine})]$ (M = Ru, Os).[17,53] At room temperature, the dianion $\mathbf{3b}^{2-}$ was, however, not detectable on the reverse scan (vide infra). Instead, scan reversal behind R_1 resulted in the appearance of an anodic peak at –1.17 V (O_2') assigned, in accordance with the results for $[Os_3(CO)_{10}(i\text{Pr-PyCa})]$,[53] to the oxidation of the cluster dimer $[^{-}Os(CO)_4\text{–}Os(CO)_4\text{–}Ru(CO)_2(i\text{Pr-AcPy})]_2^{2-}$ ($[\mathbf{3b\text{-}3b}]^{2-}$) containing an (*i*Pr-AcPy)Ru–Ru(*i*Pr-AcPy) bond. Additional proof for this assignment was obtained from IR spectroelectrochemical experiments (vide infra), where the reduction of **3** resulted in the appearance of a ν(CO) band pattern closely resembling that of the photogenerated zwitterions with an open cluster core. On lowering the temperature to 200 K, the reduction of **3** remained chemically irreversible (Figure 14b). However, in contrast to the room-temperature scan, the anodic sweep showed an additional anodic peak at –1.50 V (O_2) assigned[53] to the oxidation of $\mathbf{3b}^{2-}$, the latter species being sufficiently stable at low temperatures. The minor anodic process denoted with the asterisk (Figure 14b) corresponds to the oxidation of unassigned species.

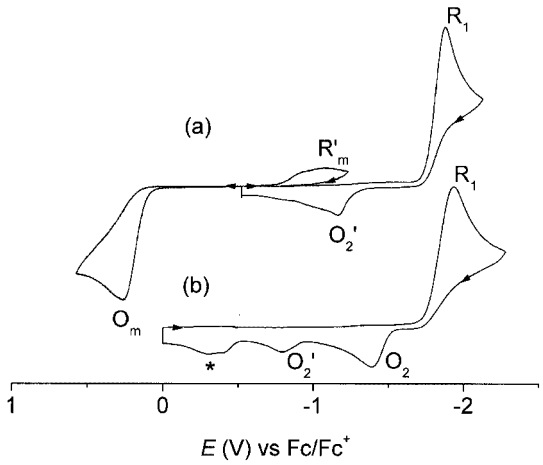

Figure 14. Cyclic voltammogram of cluster **3** at T = 293 K (a) and T = 200 K (b). Conditions: 10^{-3} M cluster in THF/10^{-1} M Bu_4NPF_6, Pt disk microelectrode (0.42 mm^2 apparent surface area), v = 100 mV s^{-1}.

Cyclic voltammetry thus documents that the closed-triangle radical anion of **3** cannot be stabilised even at 200 K and readily transforms into the open-structure dianion $\mathbf{3b}^{2-}$ (see Scheme 3). The latter dianion is also unstable and could only be produced in detectable amounts at low temperatures. This is in contrast with the results of $[Os_3(CO)_{10}(i\text{Pr-PyCa})]$, where the oxidation of the open-structure dianion is already clearly visible at 293 K.[53] Formation of dimer $[\mathbf{3b\text{-}3b}]^{2-}$, whose oxidation is observed at 200 K at $E_{p,a}$ = –0.85 V (O_2'), is known to take place by a rapid nucleophilic attack of dianion $\mathbf{3b}^{2-}$ at the yet nonreduced parent cluster **3**. A similar ECEC reduction path, for example, has been reported for the homonuclear clusters $[Os_3(CO)_{10}(\alpha\text{-diimine})]$.[53] Both $\mathbf{3b}^{2-}$ and $[\mathbf{3b\text{-}3b}]^{2-}$ are structurally related to the solvent-stabilised zwitterions

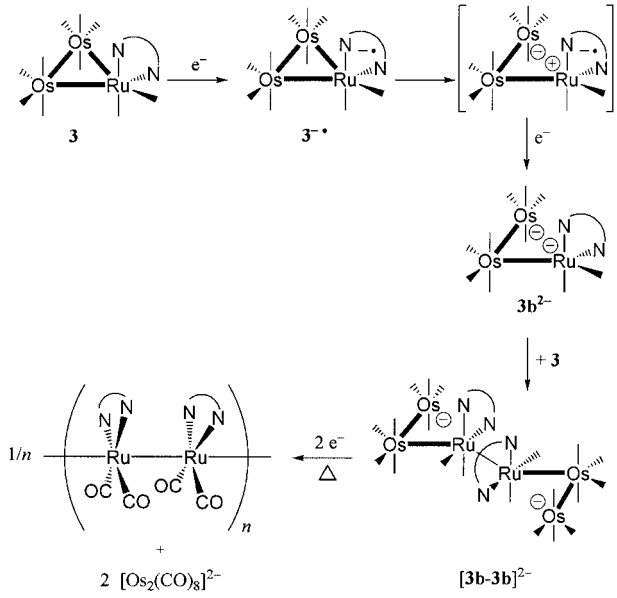

Scheme 3. Reduction path of cluster **3**.

[$^{-}$Os(CO)$_4$–Os(CO)$_4$–$^{+}$Ru(Sv)(CO)$_2$(*i*Pr-AcPy)], the photoproduct of **3** in coordinating solvents (Sv) (vide supra).

For completeness, the oxidation of cluster **3** at the potential $E(O_m)$ is chemically irreversible, resulting in a secondary product reducible on the reverse cathodic scan at the potential $E(R'_m)$. These processes were not studied in detail.

In the course of corresponding IR spectroelectrochemical experiments, the reduction of **3** in THF at 250 K resulted in the appearance of transient ν(CO) bands at 2049 (m), 2009 (m), 1991 (m), 1965 (s), 1942 (sh) and 1864 (m) cm^{-1}, similarly to the IR ν(CO) spectrum reported for the open-core dimers [$^{-}$Ru(CO)$_4$–Ru(CO)$_4$–Ru(CO)$_2$(α-diimine)]$_2^{2-}$ (α-diimine = 2,2′-bipyridine, 2,2′-bipyrimidine).[17] Accordingly, these bands are assigned to the heteronuclear analogue [$^{-}$Os(CO)$_4$–Os(CO)$_4$–Ru(CO)$_2$(*i*Pr-AcPy)]$_2^{2-}$ ([**3b-3b**]$^{2-}$, Scheme 3). No IR bands attributable to the open-structure dianion **3b**$^{2-}$ were observed in the course of the reduction. This means that **3b**$^{2-}$ is unstable on the spectroelectrochemical time scale at 250 K and readily reacts with the parent cluster **3** to form the dimer [**3b-3b**]$^{2-}$. Actually, the latter species was also unstable and converted into another carbonyl product absorbing at 1938 (s) and 1863 (s, br) cm^{-1}. In agreement with the literature[31] and the results for [Os$_3$(CO)$_{10}$(α-diimine)],[60] this product is proposed to be the dinuclear complex [Os$_2$(CO)$_8$]$^{2-}$. As the highest-frequency ν(CO) band of the corresponding [Ru$_2$(CO)$_8$]$^{2-}$ complex is found at significantly lower wavenumber (Ru: 1930 cm^{-1} vs. Os: 1940 cm^{-1}),[31] the observation of [Os$_2$(CO)$_8$]$^{2-}$ provides another evidence that the α-diimine ligand in **3** is coordinated at ruthenium. Parallel to [Os$_2$(CO)$_8$]$^{2-}$, reduction of [**3b-3b**]$^{2-}$ most likely results in the formation of the polymeric chain [Ru(CO)$_2$(*i*Pr-AcPy)]$_n$, as indicated by the formation of a blue film at the working electrode and in its vicinity. Similar species are also formed as the ultimate reduction products of the clusters [M$_3$(CO)$_{10}$(α-diimine)] (M = Ru, Os), closely resembling [M(CO)$_2$(bpy)]$_n$, generated by electrochemical reduction of mononuclear complexes *trans*(Cl)-[M(CO)$_2$(bpy)(Cl)$_2$].[61–64]

The interest in these open-chain polymers [M(CO)$_2$(α-diimine)]$_n$ (M = Ru, Os) mainly derives from their electrocatalytic activity towards reduction of carbon dioxide.[63,65–67]

From the DFT results (Table 5, Figure 6) it is clear that the LUMO of cluster **3** is for about 65% the lowest π*(*i*Pr-AcPy) orbital. Further, the LUMO has also got a nonnegligible σ*(Ru–Os2) character. Single occupation of this orbital is therefore expected to result in largely α-diimine-localised radical anion **3**$^{\cdot-}$ with a weakened Ru–Os2 bond. This bond becomes readily cleaved, similar to the photoreactivity of cluster **3** (vide supra). While the photochemical cleavage is promoted by the partial σσ* character of the excited state, the driving force behind the electrochemical cleavage is probably the pronounced donor nature of the singly reduced *i*Pr-AcPy ligand in **3**$^{\cdot-}$ causing strong polarisation of the Ru–Os2 bond nearly perpendicular to the *i*Pr-AcPy plane. Unlike the corresponding homonuclear clusters [Os$_3$(CO)$_{10}$(*i*Pr-PyCa)][53] and [Ru$_3$(CO)$_8$(μ-CO)$_2$(α-diimine)][17] [α-diimine = 2,2′-bipyridine (bpy), 4,4′-dimethyl-2,2′-bipyridine (dmb), 2,2′-bipyrimidine (bpym)] forming fairly stable radical anions at moderately low temperatures, the reduction of **3** remains chemically irreversible even at 200 K. A comparison of the reduction potentials of the homonuclear [M$_3$(CO)$_{10}$(α-diimine)] clusters (M = Os,[68] Ru[17]) with that of **3** (–1.87 V) reveals that the π-acceptor capacity of the *i*Pr-AcPy ligand in **3** is similar to that of bpy (–1.85 V, M = Os, Ru) and dmb (–1.91 V, M = Ru). This implies that the higher reactivity of radical anions **3**$^{\cdot-}$ is not due to a limited donor power of the reduced *i*Pr-AcPy ligand but, probably, has its origin in the weak heterometallic Os2–Ru(*i*Pr-AcPy) bond.

Just as for the corresponding [Os$_3$(CO)$_{10}$(*i*Pr-PyCa)] cluster,[53] no open-structure dianions were detected by IR spectroscopy on the spectroelectrochemical time scale of minutes at 250 K, the dimer [**3b-3b**]$^{2-}$ being the initially observed reduction product. The triangular open-structure units in dimer [**3b-3b**]$^{2-}$ undergo fragmentation and linear chains [Ru(CO)$_2$(*i*Pr-AcPy)]$_n$ are ultimately formed, together with the dinuclear complex [Os$_2$(CO)$_8$]$^{2-}$.

Conclusions

Crystal structures of the novel clusters [Os$_2$Ru(CO)$_{11}$(PPh$_3$)] (**2**) and [Os$_2$Ru(CO)$_{10}$(*i*Pr-AcPy)] (**3**) clearly reveal, in agreement with DFT calculations on several structural isomers, that both PPh$_3$ and *i*Pr-AcPy prefer coordination at the ruthenium site of [Os$_2$Ru(CO)$_{12}$] (**1**). The Os2–Ru(*i*Pr-AcPy) bond in cluster **3** is weaker than the corresponding metal–metal(α-diimine) bonds in the homonuclear [Os$_3$(CO)$_{10}$(*i*Pr-AcPy)] and doubly CO-bridged triruthenium analogues. This factor contributes to the observed differences in the photo- and electrochemical reactivity of cluster **3** compared to the homonuclear cores; although, the general course of the photo- and redox reactions remains unchanged.

Regarding the photochemical formation of biradical and zwitterionic photoproducts, cluster **3** closely resembles its homonuclear analogue [Os$_3$(CO)$_{10}$(*i*Pr-AcPy)]. In weakly coordinating 2-ClBu, the lowest σπ* excited state decays with a lifetime of approximately 10 ps, resulting in the formation of solvent-stabilised biradicals. In contrast to its triosmium analogue, irradiation of **3** in coordinating solvents exclusively results in heterolytic splitting of the Os2–Ru(*i*Pr-AcPy) bond, producing solvent-stabilised zwitterions. Interestingly, the lifetimes of the biradical- and zwitterionic photoproducts of cluster **3** are significantly shorter than their triosmium counterparts. This difference results most likely from a lower tendency of the coordinatively unsaturated $^{+}$Ru(CO)$_2$(*i*Pr-AcPy$^{\cdot-/0}$) moieties in the photoproducts to bind a Lewis base. Electrochemically, the influence of the weak Os2–Ru(α-diimine) bond is clearly reflected in the low stability of the radical anions initially formed by one-electron reduction of **3**.

In general, the combination of experimental photo- and electrochemical techniques together with the theoretical support from DFT calculations have provided a good in-

sight into the bonding properties of $[Os_2Ru(CO)_{10}(i$PrAcPy)]. Although the incorporation of a Ru centre into the cluster core does not induce drastic changes in the photo- and electrochemical reactivity pattern in comparison with the triosmium derivative, more pronounced heterosite effects may, for example, be expected for mixed-metal clusters combining transition metal centres from different groups of the periodic Table (e.g., Os_2Pt, Os_2Rh).

Experimental Section

Materials and Preparations: Solvents of analytical grade [Acros: acetone, acetonitrile (MeCN), dichloromethane (CH_2Cl_2), hexane, tetrahydrofuran (THF); Aldrich: 2-Chlorobutane (2-ClBu); Merck: pyridine] were dried with sodium wire (hexane), sodium/benzophenone (THF), $CaSO_4$ (acetone) and CaH_2 (MeCN, CH_2Cl_2, 2-ClBu, pyridine) and freshly distilled under nitrogen prior to use. $[Ru_3(CO)_{12}]$, $[Os_3(CO)_{12}]$ (Strem Chemicals), PPh_3, Br_2 (Aldrich), ferrocene (BDH) and NH_3 (Praxair) were used as received. Trimethylamine *N*-oxide, $Me_3NO{\cdot}2H_2O$ (Janssen), was dehydrated before use by vacuum sublimation. The supporting electrolyte Bu_4NPF_6 (Aldrich) was recrystallised twice from ethanol and dried in vacuo at 350 K overnight. Neutral aluminium oxide 90 (70–230 mesh, Merck) and silica 60 (70–230 mesh, Merck) for column chromatography were activated by heating in vacuo at 450 K overnight and stored under N_2. Preparative TLC was performed on Silica Gel G plates (20×20 cm, 1 μm, Analtech).

Synthetic Procedures: All syntheses were performed under dry nitrogen, using standard Schlenk techniques. The preparation of $Na_2[Ru(CO)_4]$ and the consecutive coupling with $[Os_2(CO)_8(Br)_2]$ were performed on a high-vacuum line at reduced pressure ($\approx 10^{-4}$ Pa). $[Os_3(CO)_{12}(Br)_2]$,[69] $[Os_2(CO)_8(Br)_2]$[30] and $Na_2[Ru(CO)_4]$[31] were prepared by modified literature procedures. $[Os_2Ru(CO)_{11}(MeCN)]$ and $[Os_2Ru(CO)_{10}(MeCN)_2]$ were prepared by similar procedures as used by Foulds et al. for the syntheses of $[Ru_3(CO)_{12-n}(MeCN)_n]$ (n = 1, 2).[70] Both clusters were prepared in situ and only characterised by IR spectroscopy (vide infra).

Synthesis of $[Os_3(CO)_{12}(Br)_2]$: In a typical experiment, a solution of $[Os_3(CO)_{12}]$ (500 mg, 0.55 mmol) in CH_2Cl_2 (350 mL) was heated to reflux for 20 min. After addition of Br_2 (40 μL, 0.78 mmol) the solvent was immediately removed in vacuo. The pale yellow residue was dissolved in CH_2Cl_2/hexane, 1:4 (400 mL) and precipitated at 190 K. The product was obtained as a pale yellow powder (412 mg, 70%) and used in the synthesis of $[Os_2(CO)_8(Br)_2]$ without further purification. IR (CH_2Cl_2): $\tilde{\nu}$ [ν(CO)] = 2149 (vw), 2119 (s), 2062 (vs, br), 2030 (s), 2002 (w) cm^{-1}.

Synthesis of $[Os_2(CO)_8(Br)_2]$: A solution of $[Os_3(CO)_{12}(Br)_2]$ (350 mg, 0.33 mmol) in CH_2Cl_2 (60 mL) was heated at 323 K to dissolve all starting material. After cooling to room temperature, Br_2 (14.5 μL, 0.28 mmol) was added and the solution was irradiated with a 125 W high-pressure Hg lamp using a $\lambda > 420$ nm cut-off filter. The reaction was monitored by IR spectroscopy and irradiation was stopped when no further increase of the product ν(CO) bands was observed (ca. 85% conversion). After removal of the solvent in vacuo, the crude yellow product was extracted with hexane (5×10 mL). The combined fractions were filtered and the solvents evaporated to dryness. The remaining solid was redissolved in hexane containing a few drops of CH_2Cl_2 and precipitated at 270 K. The product was obtained as a pale yellow powder (86 mg, 40%). IR (hexane): $\tilde{\nu}$ [ν(CO)] = 2118 (s), 2079 (vs), 2067 (s), 2063 (vs), 2052 (s), 2031 (s) cm^{-1}.

Synthesis of $Na_2[Ru(CO)_4]$ and $[Os_2Ru(CO)_{12}]$ (1): Two reaction vessels, equipped with Rotaflo® stopcocks and connected by a glass frit, were placed on a standard high-vacuum line. Under a continuous N_2 flow, $[Os_2(CO)_8(Br)_2]$ (200 mg, 0.26 mmol) was placed in one of the vessels while the other one contained $[Ru_3(CO)_{12}]$ (55.8 mg, 0.087 mmol) and metallic sodium (12 mg, 0.52 mmol). Anhydrous NH_3 (ca. 25 mL) was condensed in a separate vessel onto metallic sodium and frozen, using a liquid nitrogen bath. After closing the vessel containing $[Os_2(CO)_8(Br)_2]$, NH_3 was distilled under vacuum onto the sodium/$[Ru_3(CO)_{12}]$ mixture. Using an acetone/dry ice bath, the solution was slowly warmed to 235 K and stirred vigorously until the characteristic blue Na/NH_3 solution transformed into a yellow solution containing a white precipitate. This usually required about 30 minutes of reaction time. The mixture was stirred for another 30 minutes and remaining sodium, which splashed on the walls of the flask, was washed down by cold spotting with glass wool drenched with liquid nitrogen. After 1 h, NH_3 was evaporated by further warming to 260 K and the remaining cream-coloured solid was dried under high-vacuum conditions for another 3.5 h at this temperature. $Na_2[Ru(CO)_4]$ was then dissolved on the vacuum line in THF that had been pre-dried with sodium/benzophenone and thoroughly degassed in four consecutive freeze-pump-thaw cycles. The pale yellow solution was degassed once more to remove the last traces of ammonia. Finally, the THF solution was warmed to 273 K and added to $[Os_2(CO)_8(Br)_2]$ by filtration through the frit connecting the reaction vessels. Upon mixing, the solution turned red and gas was evolving. The solution was stirred overnight at 293 K, followed by evaporation of the solvent. Purification of the crude product was established by column chromatography (activated neutral alumina, hexane/CH_2Cl_2 gradient elution). After precipitation from THF at 190 K, the product was obtained as a yellow powder in yields varying between 86 and 135 mg (40–63% based on $[Os_2(CO)_8(Br)_2]$), depending on the quality of $Na_2[Ru(CO)_4]$ (vide supra). IR (hexane): $\tilde{\nu}$ [ν(CO)] = 2068(s), 2036 (s), 2015 (m), 2004 (m) cm^{-1}. UV/Vis (CH_2Cl_2): λ = 280 (sh), 329, 382 (sh) nm. MS (FD): m/z = 817 $[M]^+$ (calcd. 817.8). MS (EI): $m/z = [M^+ - n\text{CO}]$ (n = 0–12).

Synthesis of $[Os_2Ru(CO)_{11}(PPh_3)]$ (2): Me_3NO (5.5 mg, 0.07 mmol) in MeCN (2 mL) was added to a solution of $[Os_2Ru(CO)_{12}]$ (30 mg, 0.04 mmol) in THF (25 mL) at 200 K. After stirring the mixture for approximately 30 minutes, IR spectra revealed almost complete conversion to $[Os_2Ru(CO)_{11}(MeCN)]$. After addition of PPh_3 (10.6 mg, 0.04 mmol), the solution was warmed to room temperature. As IR spectra showed hardly any conversion after 60 minutes, additional PPh_3 was added (5.2 mg, 0.02 mmol) and the solution was stirred for two days in the dark. After removal of the solvent in vacuo, the residue was loaded on a silica 60 column packed in hexane. Gradient elution with hexane/THF resulted in the clean separation of three (yellow, orange and red) mobile bands. The yellow fraction was further purified by preparative TLC to remove free PPh_3. Recrystallisation of the yellow residue from petroleum ether 40–60 at 250 K yielded orange crystals of cluster **2** (15 mg, 40%). On the basis of their IR spectra, the orange and red fractions likely contained higher substituted compounds, but no detailed characterization of the mixtures was attempted.

$[Os_2Ru(CO)_{11}(MeCN)]$: IR (CH_2Cl_2): $\tilde{\nu}$ [ν(CO)] = 2104 (w), 2050 (vs), 2040 (vs), 2019 (s, sh), 2008 (vs), 1984 (m) cm^{-1}.

$[Os_2Ru(CO)_{11}(PPh_3)]$ (2): IR (CH_2Cl_2): $\tilde{\nu}$ [ν(CO)] = 2107 (m), 2054 (s), 2033 (s), 2017 (vs), 1999 (m), 1988 (m), 1977 (m), 1957 (w) cm^{-1}. ^1H NMR (300 MHz, $CDCl_3$, 293 K): δ = 7.35 (m, 15

H) ppm. $^{31}P\{H\}$ NMR (300 MHz, $CDCl_3$, 293 K): δ = 29.6 ([$Os_2Ru(CO)_{11}(PPh_3)$]), –0.8 ([$Os_3(CO)_{11}(PPh_3)$]) ppm (ratio ca. 2:1). MS (FD): m/z = 1142 $[M]^+$ (M = [$Os_3(CO)_{11}(PPh_3)$]) (calcd. 1141.9), 1054 $[M]^+$ (M = [$Os_2Ru(CO)_{11}(PPh_3)$]) (calcd. 1053.9) (ratio ca.1:2).

Synthesis of [$Os_2Ru(CO)_{10}$(*i*Pr-AcPy)] (3): To a solution of [$Os_2Ru(CO)_{11}$(MeCN)] at 270 K, freshly prepared from [$Os_2Ru(CO)_{12}$] (100 mg, 0.12 mmol) and Me_3NO (18.6 mg, 0.25 mmol), a solution of Me_3NO (13.5 mg, 0.18 mmol) in CH_2Cl_2 was added dropwise. After stirring for 45 minutes IR spectra revealed [$Os_2Ru(CO)_{10}$(MeCN)$_2$] as the main product. After addition of *i*Pr-AcPy (200 mg, 1.2 mmol) the solution was stirred overnight while warming to room temperature. Purification of the crude product over silica using 2:3 hexane/THF as eluent gave [$Os_2Ru(CO)_{10}$(*i*Pr-AcPy)] as a purple powder (34 mg, 30%). Crystals were grown by slow diffusion of hexane into a saturated solution of [$Os_2Ru(CO)_{10}$(*i*Pr-AcPy)] in THF.

[$Os_2Ru(CO)_{10}$(MeCN)$_2$]: IR (CH_2Cl_2): $\tilde{\nu}$ [ν(CO)] = 2079 (w), 2019 (vs), 1984 (s), 1958 (m) cm^{-1}.

[$Os_2Ru(CO)_{10}$(*i*Pr-AcPy)] (3): IR (THF): $\tilde{\nu}$ [ν(CO)] = 2082 (m), 2028 (vs), 2002 (vs), 1990 (s), 1979 (s), 1962 (m), 1956 (sh), 1907 (w) cm^{-1}. ^1H NMR (300 MHz, $CDCl_3$, 293 K) {for numbering scheme see Figure 1; asterisks denote signals due to [$Os_3(CO)_{10}$(*i*Pr-AcPy)] (ca.10–15%)}: δ = 9.50* (d, 1 H), 9.23 (d, $^3J_{H,H}$ = 4.5 Hz, 1 H, H^6), 8.04 (d, $^3J_{H,H}$ = 8.1 Hz, 1 H, H^3), 8.02* (d, 1 H), 7.91 (dd, $^3J_{H,H}$ = 8.1, $^3J_{H,H}$ = 7.5 Hz, 1 H, H^4), 7.86* (dd, 1 H), 7.25 (dd, $^3J_{H,H}$ = 7.5, $^3J_{H,H}$ = 5 Hz, 1 H, H^5), 7.11* (dd, 1 H), 4.44* (m, 1 H), 3.73 (m, 1 H, C*H*(CH_3)$_2$), 2.66 (s, 3 H, N=C–C*H*$_3$), 1.40 [d, $^3J_{H,H}$ = 4.8 Hz, 6 H, CH(C*H*$_3$)$_2$] ppm. MS (FAB^+): m/z = 986.9 $[M + H]^+$–CO (M = [$Os_3(CO)_{10}$(*i*Pr-AcPy)]), 957.9 $[M + H]^+$ – 2CO (M = [$Os_3(CO)_{10}$(*i*Pr-AcPy)]), 925.91 $[M + H]^+$ (M = [$Os_2Ru(CO)_{10}$(*i*Pr-AcPy)]) (calcd. 925.89), $[M + H]^+$–*n*CO (n = 1–10) (M = [$Os_2Ru(CO)_{10}$(*i*Pr-AcPy)]).

X-ray Crystal Structure Determinations of Clusters 2 and 3: Intensities were measured with a Nonius KappaCCD diffractometer with rotating anode (Mo-K_α, λ = 0.71073 Å) at a temperature of 150(2) K up to a resolution of ($\sin\theta/\lambda$) = 0.65 $Å^{-1}$. The structures were solved with Patterson methods (DIRDIF-97)[71] and refined with the programme SHELXL-97[72] against F^2 of all reflections. Non-hydrogen atoms were refined freely with anisotropic displacement parameters, and hydrogen atoms as rigid groups. The drawings, structure calculations, and checking for higher symmetry were performed with the programme PLATON.[73] The ruthenium sites in both structures were partially occupied by osmium atoms. The ruthenium and the corresponding osmium atoms were constrained to the same coordinates and the same anisotropic displacement parameters. Then the partial occupancies were refined with the criterion that the total occupancy remains 1.0.

[$Os_2Ru(CO)_{11}(PPh_3)$] (2): $C_{29}H_{15}O_{11}Os_{2.36}PRu_{0.64}$; Fw = 1083.94; yellow plates, 0.36 × 0.21 × 0.12 mm^3; monoclinic, space group $C2/c$ (no. 15); cell parameters: a = 21.9824(1), b = 16.0859(1) Å, c = 17.2605(1) Å; β = 103.7064(3)°; V = 5929.62(6) $Å^3$; Z = 8; ρ = 2.428 g cm^{-3}; F(000) = 3996; 55381 reflections were measured, 6811 reflections were unique (R_{int} = 0.0519). An analytical absorption correction was applied (μ = 10.526 mm^{-1}, 0.08–0.39 transmission). 398 Refined parameters, no restraints. R (obsd. refl.): R_1 = 0.0196, wR_2 = 0.0425. R (all data): R_1 = 0.0230, wR_2 = 0.0434. Weighting scheme $w = 1/[\sigma^2(F_o^2) + (0.0165P)^2 + 11.6188P]$, where $P = (F_o^2 + 2F_c^2)/3$. GoF = 1.110. Residual electron density between –0.92 and 0.75 e/$Å^3$.

[$Os_2Ru(CO)_{10}$(*i*Pr-AcPy)] (3): $C_{20}H_{14}N_2O_{10}Os_{2.11}Ru_{0.89}$; Fw = 933.61; red needles, 0.39 × 0.03 × 0.03 mm^3; monoclinic, space group $P2_1/c$ (no. 14); cell parameters: a = 9.1117(1), b = 13.9915(1) Å, c = 20.7504(2) Å; β = 113.6862(4)°; V = 2422.54(4) $Å^3$; Z = 4; ρ = 2.560 g cm^{-3}; F(000) = 1710. 43532 reflections were measured, 5551 reflections were unique (R_{int} = 0.0740). An analytical absorption correction was applied (μ = 11.644 mm^{-1}, 0.20–0.78 transmission). 320 refined parameters, no restraints. R (obsd. refl.): R_1 = 0.0277, wR_2 = 0.0419. R (all data): R_1 = 0.0510, wR_2 = 0.0460. Weighting scheme $w = 1/[\sigma^2(F_o^2) + (0.0147P)^2]$, where $P = (F_o^2 + 2F_c^2)/3$. GoF = 0.996. Residual electron density between –0.95 and 1.01 e/$Å^3$.

CCDC-258240 (for **2**) and -258241 (for **3**) contain the supplementary crystallographic data for this paper. These data can be obtained free of charge from The Cambridge Crystallographic Data Centre via www.ccdc.cam.ac.uk/data_request/cif.

Spectroscopic Measurements: Electronic absorption spectra were recorded with a Hewlett–Packard 8453 diode-array spectrophotometer and FT-IR spectra with a Bio-Rad FTS-7 (16 scans at 2 cm^{-1} resolution) spectrometer. Rapid-scan FT-IR spectra were measured with a Bio-Rad FTS-60A spectrometer (equipped with a dual-source rapid-scan 896 interferometer and a liquid-nitrogen cooled MCT detector) after excitation of the sample by the 514.5 nm line of a Spectra Physics Model 2016 argon-ion laser. ^1H and $^{31}P\{H\}$ NMR spectra were recorded with a Bruker AMX 300 spectrometer. Field Desorption (FD), Fast Atom Bombardment (FAB) and Electron Impact (EI) mass spectra were collected with a JEOL JMS SX/SX102A four-sector mass spectrometer. For synthetic purposes, a Philips HPK 125-W high-pressure Hg lamp, equipped with appropriate cut-off filters to select the desired wavelength region, served as a light source.

Photochemistry: All photochemical samples were prepared under nitrogen, using standard inert-gas techniques, and cluster concentrations typically between 10^{-3}–10^{-4} mol·dm^{-3}. Nanosecond transient absorption (ns TA) spectra were obtained by irradiating the samples with 2 ns pulses of the 532 nm line (typically 5 mJ $pulse^{-1}$) of a tunable (420–710 nm) Coherent Infinity XPO laser and using a high-power EG&G FX-504 Xe lamp as probe light.[17] Nanosecond flash photolysis transient kinetics were measured by irradiating the sample with 7 ns (FWHM) pulses of a Spectra Physics GCR-3 Nd:YAG laser (10 Hz repetition rate) and using a pulsed Xe lamp perpendicular to the laser beam as probe light. The excitation wavelength in this case (532 nm) was obtained by frequency doubling. The 450-W Xe lamp was equipped with a Müller Electronik MSP05 pulsing unit, giving pulses of 0.5 ms. A shutter, placed between the lamp and the sample, was opened for 10 ms to prevent photomultiplier fatigue. Suitable pre- and post-cut-off filters and band-pass filters were used to minimize both the probe light and scattered light from the laser. The sampling rate was kept at a relatively long time (10 s intervals) to prevent accumulation of possible photo-induced intermediates. The light was collected in an Oriel monochromator, detected by a P28 PMT (Hamamatsu), and recorded with a Tektronix TDS3052 (500 MHz) oscilloscope. The laser oscillator, Q-switch, lamp, shutter and trigger were externally controlled with a home made digital logic circuit, which allowed for synchronous timing. The absorption transient were plotted as $\Delta A = \log(I_t/I_0)$ vs. time, where I_0 is the monitoring light intensity prior to the laser pulse and I_t is the observed signal at delay time t.

Picosecond transient absorption (ps TA) spectra were recorded using the set-up installed at the University of Amsterdam.[16] Part of the 800 nm output of a Ti-sapphire regenerative amplifier (1 kHz, 130 fs, 1 mJ) was focussed into a H_2O flow-through cell (10 mm; Hellma) to generate white light. The residual part of the

800 nm fundamental was used to provide 505 nm (fourth harmonic of the 2020 OPA idler beam) excitation pulses with a general output of 5 μJ pulse^{-1}. After passing through the sample, the probe beam was coupled into a 400 μm optical fibre and detected by a CCD spectrometer (Ocean Optics, PC2000). The chopper (Rofin Ltd., f = 10–20 Hz), placed in the excitation beam, provided I and I_0, depending on the status of the chopper (open or closed). The excited state spectra were obtained by $\Delta A = \log(I/I_0)$. Typically two thousand excitation pulses were averaged to obtain the transient at a particular time delay.

Electrochemistry: Cyclic voltammograms (CV) of approximately 10^{-3} M parent cluster in 10^{-1} M Bu_4NPF_6 electrolyte solution were recorded in a gas-tight, single-compartment, three-electrode cell equipped with platinum microdisc (apparent surface 0.42 mm^2) working, coiled platinum wire auxillary and silver wire pseudo-reference electrodes. The cell was connected to a computer-controlled PAR Model 283 potentiostat. All redox potentials are reported against the ferrocene-ferrocenium (Fc/Fc^+) redox couple.[74,75] IR spectroelectrochemical measurements at variable temperatures were performed with previously described optically transparent thin-layer electrochemical (OTTLE) cells[76,77] equipped with a platinum minigrid working electrode (32 wires/cm) and CaF_2 windows. The potential during these measurements was controlled by a PA4 potentiostat (EKOM, Czech Republic). In the spectroelectrochemical experiments, cluster concentrations of 5×10^{-3} mol·dm^{-3} were used.

Computational Details: All density functional theory (DFT) calculations[78] were carried out with the Amsterdam Density Functional (ADF2000) programme.[37–43] Vosko, Wilk and Nusair's local exchange correlation potential was used.[79] Gradient-corrected geometry optimizations[80,81] were performed, using the Generalized Gradient Approximation (Becke's exchange[82] and Perdew's correlation[83,84] functionals). Relativistic effects were treated by the ZORA method[85] The core orbitals were frozen for Ru ([1–4]s, [2–4]p, 3d), Os ([1–4]s, [2–4]p, [3–4]d), P ([1–2]s, 2p), and C, N, O (1s). Triple ζ Slater-type orbitals (STO) were used to describe the valence shells of H (1s), C and O (2s and 2p), P (3s and 3p), Ru (4d, 5s and 5p) and Os (4f, 5d, 6s). A set of polarization functions was added: H (single ζ, 2p, 3d), C, N, O (single ζ, 3d, 4f), P(single ζ, 3d, 4f), Ru (single ζ, 5p, 4f) and Os (single ζ, 6p, 5f). Full geometry optimizations were performed without any symmetry constraints on models based on the available crystal structures. The UV/Vis spectrum was calculated using the SWizard programme,[48] revision 3.7. The half-band widths, $\Delta_{1/2,I}$, were taken to be equal to 3000 cm^{-1}, the default value of the programme. Three-dimensional representations of the orbitals were obtained with Molekel.[86]

Time-dependent DFT (TD-DFT)[87–89] calculations in the ADF implementation were used to determine the excitation energies. In all cases the ten lowest singlet-singlet excitation energies were calculated using the optimized geometries.

Acknowledgments

A. Hearley (University of Cambridge, UK) is gratefully acknowledged for valuable discussions regarding the synthesis of [$Os_2Ru(CO)_{12}$]. This work was undertaken as part of the European collaborative COST project (D14/0001/99). Financial support was received by F. W. V. and F. H. from the Council for Chemical Sciences of the Netherlands Organization for Scientific Research (CW-NWO, project No. 348–032).

[1] R. D. Adams, in *Comprehensive Organometallic Chemistry II*, vol. 10, Pergamon, New York, **1995**.
[2] W. L. Gladfelter, G. L. Geoffroy, *Adv. Organomet. Chem.* **1980**, *18*, 207–273.
[3] D. A. Roberts, G. L. Geoffroy, in *Comprehensive Organometallic Chemistry*, vol. 6, Pergamon, Oxford, **1982**.
[4] S. M. Waterman, N. T. Lucas, M. G. Humphrey, *Adv. Organomet. Chem.* **2000**, *46*, 47–143.
[5] P. Braunstein, J. Rosé, in *Catalysis by Di- and Polynuclear Metal Cluster Complexes* (Eds.: R. D. Adams, F. A. Cotton), Wiley-VCH, New York, **1998**, pp. 443–508.
[6] P. Braunstein, J. Rosé, in *Comprehensive Organometallic Chemistry II*, vol. 10, Pergamon, New York, **1995**.
[7] R. D. Adams, T. S. Barnard, Z. Li, W. Wu, J. H. Yamamoto, *J. Am. Chem. Soc.* **1994**, *116*, 9103–9113.
[8] M. A. Aubart, L. H. Pignolet, *J. Am. Chem. Soc.* **1992**, *114*, 7901–7903.
[9] S. Attali, R. Mathieu, *J. Organomet. Chem.* **1985**, *291*, 205–211.
[10] I. Ojima, Z. Zhang, *J. Org. Chem.* **1988**, *53*, 4422–4425.
[11] L. J. Farrugia, in *Comprehensive Organometallic Chemistry II*, vol. 10, Pergamon, New York, **1995**.
[12] J. Nijhoff, M. J. Bakker, F. Hartl, D. J. Stufkens, W.-F. Fu, R. van Eldik, *Inorg. Chem.* **1998**, *37*, 661–668.
[13] J. Nijhoff, F. Hartl, D. J. Stufkens, J. Fraanje, *Organometallics* **1999**, *18*, 4380–4389.
[14] J. Nijhoff, M. J. Bakker, F. Hartl, D. J. Stufkens, *J. Organomet. Chem.* **1999**, *572*, 271–281.
[15] M. J. Bakker, F. Hartl, D. J. Stufkens, O. S. Jina, X.-Z. Sun, M. W. George, *Organometallics* **2000**, *19*, 4310–4319.
[16] F. W. Vergeer, C. J. Kleverlaan, D. J. Stufkens, *Inorg. Chim. Acta* **2002**, *327*, 126–133.
[17] F. W. Vergeer, M. J. Calhorda, P. Matousek, M. Towrie, F. Hartl, *Dalton Trans.* **2003**, 4084–4099.
[18] M. J. Calhorda, E. Hunstock, L. F. Veiros, F. Hartl, *Eur. J. Inorg. Chem.* **2001**, 223–231.
[19] M. J. Calhorda, P. J. Costa, F. Hartl, F. W. Vergeer, *C. R. Chimie* **2005**, in the press.
[20] E. Hunstock, C. Mealli, M. J. Calhorda, J. Reinhold, *Inorg. Chem.* **1999**, *38*, 5053–5060.
[21] E. Hunstock, M. J. Calhorda, P. Hirva, T. A. Pakkanen, *Organometallics* **2000**, *19*, 4624–4628.
[22] G. A. Battiston, G. Bor, U. K. Dietler, S. F. A. Kettle, R. Rossetti, G. Sbrignadello, P. L. Stanghellini, *Inorg. Chem.* **1980**, *19*, 1961–1973.
[23] R. P. Ferrari, G. A. Vaglio, M. Valle, *J. Chem. Soc., Dalton Trans.* **1978**, 1164–1166.
[24] B. F. G. Johnson, R. D. Johnston, J. Lewis, I. G. Williams, P. A. Kilty, *Chem. Commun.* **1968**, 861–862.
[25] J. R. Fox, W. L. Gladfelter, G. L. Geoffroy, *Inorg. Chem.* **1980**, *19*, 2574–2578.
[26] H. Remita, R. Derai, M.-O. Delcourt, *Radiat. Phys. Chem.* **1991**, *37*, 221–225.
[27] J. R. Moss, W. A. G. Graham, *J. Chem. Soc., Dalton Trans.* **1977**, 89–94.
[28] B. F. G. Johnson, R. D. Johnston, P. L. Josty, J. Lewis, I. G. Williams, *Nature* **1967**, *213*, 901–902.
[29] B. F. G. Johnson, R. D. Johnston, J. Lewis, *J. Chem. Soc., A* **1969**, 792–797.
[30] J. R. Moss, M. L. Niven, E. E. Sutton, *Inorg. Chim. Acta* **1988**, *147*, 251–256.
[31] N. K. Bhattacharyya, T. J. Coffy, W. Quintana, T. A. Salupo, J. C. Bricker, T. B. Shay, M. Payne, S. G. Shore, *Organometallics* **1990**, *9*, 2368–2374.
[32] M. R. Churchill, B. G. DeBoer, *Inorg. Chem.* **1977**, *16*, 878–884.
[33] M. R. Churchill, F. J. Hollander, J. P. Hutchinson, *Inorg. Chem.* **1977**, *16*, 2655–2659.
[34] L. Pereira, W. K. Leong, S. Y. Wong, *J. Organomet. Chem.* **2000**, *609*, 104–109.
[35] M. I. Bruce, M. J. Liddell, C. A. Hughes, B. W. Skelton, A. H. White, *J. Organomet. Chem.* **1988**, *347*, 157–180.

[36] E. J. Forbes, N. Goodhand, D. L. Jones, T. A. Hamor, *J. Organomet. Chem.* **1979**, *182*, 143–154.
[37] E. J. Baerends, D. Ellis, P. Ros, *Chem. Phys.* **1973**, *2*, 41–51.
[38] E. J. Baerends, P. Ros, *Int. J. Quantum Chem.* **1978**, *S12*, 169–190.
[39] E. J. Baerends, A. Bérces, C. Bo, P. M. Boerrigter, L. Cavallo, L. Deng, R. M. Dickson, D. E. Ellis, L. Fan, T. H. Fischer, C. Fonseca Guerra, S. J. A. van Gisbergen, J. A. Groeneveld, O. V. Gritsenko, F. E. Harris, P. van den Hoek, H. Jacobsen, G. van Kessel, F. Kootstra, E. van Lenthe, V. P. Osinga, P. H. T. Philipsen, D. Post, C. C. Pye, W. Ravenek, P. Ros, P. R. T. Schipper, G. Schreckenbach, J. G. Snijders, M. Sola, D. Swerhone, G. te Velde, P. Vernooijs, L. Versluis, O. Visser, E. van Wezenbeek, G. Wiesenekker, S. K. Wolff, T. K. Woo, T. Ziegler, *ADF 2000*, University of Amsterdam, Amsterdam, **2000**.
[40] C. Fonseca Guerra, O. Visser, J. G. Snijders, G. te Velde, E. J. Baerends, in *Methods and Techniques for Computational Chemistry* (Eds.: E. Clementi, C. Corongiu), STEF, Cagliari, **1995**, pp. 303–395.
[41] C. Fonseca Guerra, J. G. Snijders, G. te Velde, E. J. Baerends, *Theor. Chem. Acc.* **1998**, *99*, 391–403.
[42] P. M. Boerrigter, G. te Velde, E. J. Baerends, *Int. J. Quantum Chem.* **1988**, *33*, 87–113.
[43] G. te Velde, E. J. Baerends, *J. Comput. Phys.* **1992**, *99*, 84–98.
[44] V. M. Hansen, A. K. Ma, K. Biradha, R. K. Pomeroy, M. J. Zaworotko, *Organometallics* **1998**, *17*, 5267–5274.
[45] N. E. Leadbeater, J. Lewis, P. R. Raithby, G. N. Ward, *J. Chem. Soc., Dalton Trans.* **1997**, 2511–2516.
[46] R. Zoet, T. B. H. Jastrzebski, G. van Koten, T. Mahabiersing, K. Vrieze, D. Heijdenrijk, C. H. Stam, *Organometallics* **1988**, *7*, 2108–2117.
[47] D. M. Manuta, A. J. Lees, *Inorg. Chem.* **1983**, *22*, 3825–3828.
[48] S. I. Gorelsky, *SWizard programme*, revision 3.7, http://www.obbligato.com/software/swizard/.
[49] B. D. Rossenaar, D. J. Stufkens, A. Vlček Jr., *Inorg. Chim. Acta* **1996**, *247*, 247–255.
[50] B. D. Rossenaar, D. J. Stufkens, A. Vlček Jr., *Inorg. Chem.* **1996**, *35*, 2902–2909.
[51] B. D. Rossenaar, E. Lindsay, D. J. Stufkens, A. Vlček Jr., *Inorg. Chim. Acta* **1996**, *250*, 5–14.
[52] M. P. Aarnts, D. J. Stufkens, M. P. Wilms, E. J. Baerends, A. Vlček Jr., I. P. Clark, M. W. George, J. J. Turner, *Chem. Eur. J.* **1996**, *2*, 1556–1565.
[53] J. Nijhoff, F. Hartl, J. W. M. van Outersterp, D. J. Stufkens, M. J. Calhorda, L. F. Veiros, *J. Organomet. Chem.* **1999**, *573*, 121–133.
[54] A. Klein, W. Kaim, *Organometallics* **1995**, *14*, 1176–1186.
[55] F. W. Vergeer, C. J. Kleverlaan, P. Matousek, M. Towrie, D. J. Stufkens, F. Hartl, *Inorg. Chem.* **2005**, 44, 1319–1331.
[56] F. P. A. Johnson, M. W. George, F. Hartl, J. J. Turner, *Organometallics* **1996**, *15*, 3374–3387.
[57] G. J. Stor, F. Hartl, J. W. M. van Outersterp, D. J. Stufkens, *Organometallics* **1995**, *14*, 1115–1131.
[58] B. D. Rossenaar, F. Hartl, D. J. Stufkens, *Inorg. Chem.* **1996**, *35*, 6194–6203.
[59] B. D. Rossenaar, F. Hartl, D. J. Stufkens, C. Amatore, E. Maisonhaute, J.-N. Verpeaux, *Organometallics* **1997**, *16*, 4675–4685.
[60] F. Hartl, J. W. M. van Outersterp, unpublished results.
[61] S. Chardon-Noblat, A. Deronzier, D. Zsoldos, R. Ziessel, M. Haukka, T. Pakkanen, T. Venäläinen, *J. Chem. Soc., Dalton Trans.* **1996**, 2581–2583.
[62] C. Caix-Cecillon, S. Chardon-Noblat, A. Deronzier, M. Haukka, T. Pakkanen, R. Ziessel, D. Zsoldos, *J. Electroanal. Chem.* **1999**, *466*, 187–196.
[63] S. Chardon-Noblat, A. Deronzier, F. Hartl, J. van Slageren, T. Mahabiersing, *Eur. J. Inorg. Chem.* **2001**, 613–617.
[64] F. Hartl, T. Mahabiersing, S. Chardon-Noblat, P. Da Costa, A. Deronzier, *Inorg. Chem.* **2004**, *43*, 7250–7258.
[65] S. Chardon-Noblat, A. Deronzier, R. Ziessel, *Collect. Czech. Chem. Commun.* **2001**, *66*, 207–226.
[66] S. Chardon-Noblat, A. Deronzier, R. Ziessel, D. Zsoldos, *J. Electroanal. Chem.* **1998**, *444*, 253–260.
[67] M.-N. Collomb-Dunand-Sauthier, A. Deronzier, R. Ziessel, *Inorg. Chem.* **1994**, *33*, 2961–2967.
[68] J. W. M. van Outersterp, Ph. D. Thesis, University of Amsterdam, Amsterdam, **1995**.
[69] B. F. G. Johnson, J. Lewis, P. A. Kilty, *J. Chem. Soc., A* **1968**, 2859–2864.
[70] G. A. Foulds, B. F. G. Johnson, J. Lewis, *J. Organomet. Chem.* **1985**, *296*, 147–153.
[71] P. T. Beurskens, G. Admiraal, G. Beurskens, W. P. Bosman, S. Carcia-Granda, R. O. Gould, J. M. M. Smits, C. Smykalla, *The DIRDIF-97 programme system*, Technical Report of the Crystallography Laboratory, University of Nijmegen, The Netherlands, **1997**.
[72] G. M. Sheldrick, *SHELXL-97*, University of Göttingen, Göttingen, Germany, **1997**.
[73] A. L. Spek, *J. Appl. Crystallogr.* **2003**, *36*, 7–13.
[74] V. V. Pavlishchuk, A. W. Addison, *Inorg. Chim. Acta* **2000**, *298*, 97–102.
[75] G. Gritzner, J. Kůta, *Pure Appl. Chem.* **1984**, *56*, 461–466.
[76] F. Hartl, H. Luyten, H. A. Nieuwenhuis, G. C. Schoemaker, *Appl. Spectrosc.* **1994**, *48*, 1522–1528.
[77] M. Krejčík, M. Daněk, F. Hartl, *J. Electroanal. Chem. Interfacial Electrochem.* **1991**, *317*, 179–187.
[78] R. G. Parr, W. Yang, *Density Functional Theory of Atoms and Molecules*, Oxford University Press, New York, **1989**.
[79] S. H. Vosko, L. Wilk, M. Nusair, *Can. J. Phys.* **1980**, *58*, 1200–1211.
[80] L. Versluis, T. Ziegler, *J. Chem. Phys.* **1988**, *88*, 322–328.
[81] L. Fan, T. Ziegler, *J. Chem. Phys.* **1991**, *95*, 7401–7408.
[82] A. D. Becke, *J. Chem. Phys.* **1988**, *88*, 1053–1062.
[83] J. P. Perdew, *Phys. Rev. B* **1986**, *33*, 8822–8824.
[84] J. P. Perdew, *Phys. Rev. B* **1986**, *34*, 7406.
[85] E. van Lenthe, A. Ehlers, E. J. Baerends, *J. Chem. Phys.* **1999**, *110*, 8943–8953.
[86] S. Portmann, H. P. Lüthi, *Chimia* **2000**, *54*, 766–770.
[87] S. J. A. van Gisbergen, J. A. Groeneveld, A. Rosa, J. G. Snijders, E. J. Baerends, *J. Phys. Chem.* **1999**, *103*, 6835–6844.
[88] S. J. A. van Gisbergen, A. Rosa, G. Ricciardi, E. J. Baerends, *J. Chem. Phys.* **1999**, *111*, 2499–2506.
[89] A. Rosa, S. J. A. van Gisbergen, E. van Lenthe, J. A. Groeneveld, J. G. Snijders, *J. Am. Chem. Soc.* **1999**, *121*, 10356–10365.

Received: December 20, 2004

